Dark Energy Survey Year 6 results: Clustering redshifts and importance sampling of self-organized-maps $n(z)$ realizations for 3×2pt samples

W. d'Assignies,[1,*] G. M. Bernstein,[2] B. Yin,[3] G. Giannini,[4,5] A. Alarcon,[6] M. Manera,[1,7] C. To,[4] M. Yamamoto,[3,8] N. Weaverdyck,[9,10] R. Cawthon,[11] M. Gatti,[5] A. Amon,[8] D. Anbajagane,[5] S. Avila,[12] M. R. Becker,[13] K. Bechtol,[14] C. Chang,[4,5] M. Crocce,[6,15] J. De Vicente,[12] S. Dodelson,[4,5,16] J. Fang,[17] A. Ferté,[18] D. Gruen,[19] E. Legnani,[1] A. Porredon,[20,21] J. Prat,[4,22] M. Rodriguez-Monroy,[23,24] C. Sánchez,[1,25] T. Schutt,[18,26,27] I. Sevilla-Noarbe,[21] D. Sanchez Cid,[21,28] M. A. Troxel,[3] T. M. C. Abbott,[29] F. Andrade-Oliveira,[28] M. Aguena,[30,31] O. Alves,[32] D. Bacon,[33] J. Blazek,[34] S. Bocquet,[19] D. Brooks,[35] R. Camilleri,[36] A. Carnero Rosell,[30,37,38] M. Carrasco Kind,[39,40] J. Carretero,[1] F. J. Castander,[5,6,15] L. N. da Costa,[30] M. E. da Silva Pereira,[41] T. M. Davis,[36] S. Desai,[42] P. Doel,[35] C. Doux,[43,2] A. Drlica-Wagner,[4,5,16] T. Eifler,[44,45] J. Elvin-Poole,[46] S. Everett,[47] B. Flaugher,[16] P. Fosalba,[6,15] J. Frieman,[4,5,16] J. García-Bellido,[48] E. Gaztanaga,[6,15,33] P. Giles,[49] G. Gutierrez,[16] S. R. Hinton,[36] D. L. Hollowood,[50] K. Honscheid,[51,52] D. Huterer,[32] B. Jain,[2] D. J. James,[53] K. Kuehn,[54,55] O. Lahav,[35] S. Lee,[45] J. L. Marshall,[56] J. Mena-Fernández,[43] F. Menanteau,[39,40] R. Miquel,[57,1] J. Muir,[58,59] J. Myles,[8] R. L. C. Ogando,[60,61] A. Palmese,[62] M. Paterno,[16] P. Petravick,[39] A. A. Plazas Malagón,[18,26] M. Raveri,[63] A. Roodman,[18,26] S. Samuroff,[1,34] E. Sanchez,[12] E. Sheldon,[64] T. Shin,[65] M. Smith,[66] E. Suchyta,[67] M. E. C. Swanson,[39] G. Tarle,[32] D. Thomas,[33] V. Vikram,[2] and A. R. Walker[29]

(DES Collaboration)

[1]*Institut de Física d'Altes Energies (IFAE), The Barcelona Institute of Science and Technology, Campus UAB, 08193 Bellaterra (Barcelona) Spain*
[2]*Department of Physics and Astronomy, University of Pennsylvania, Philadelphia, Pennsylvania 19104, USA*
[3]*Department of Physics, Duke University Durham, North Carolina 27708, USA*
[4]*Department of Astronomy and Astrophysics, University of Chicago, Chicago, Illinois 60637, USA*
[5]*Kavli Institute for Cosmological Physics, University of Chicago, Chicago, Illinois 60637, USA*
[6]*Institute of Space Sciences (ICE, CSIC), Campus UAB, Carrer de Can Magrans, s/n, 08193 Barcelona, Spain*
[7]*Barcelona, Edifici C Facultat de Ciències, 08193 Bellaterra, Spain*
[8]*Department of Astrophysical Sciences, Princeton University, Peyton Hall, Princeton, New Jersey 08544, USA*
[9]*Lawrence Berkeley National Laboratory, 1 Cyclotron Road, Berkeley, California 94720, USA*
[10]*Berkeley Center for Cosmological Physics, Berkeley, California 94720, USA*
[11]*Oxford College of Emory University, Oxford, Georgia 30054, USA*
[12]*Centro de Investigaciones Energéticas, Medioambientales y Tecnológicas (CIEMAT), Madrid, Spain*
[13]*Argonne National Laboratory, 9700 South Cass Avenue, Lemont, Illinois 60439, USA*
[14]*Physics Department, 2320 Chamberlin Hall, University of Wisconsin-Madison, 1150 University Avenue Madison, Wisconsin 53706-1390, USA*
[15]*Institut d'Estudis Espacials de Catalunya (IEEC), 08034 Barcelona, Spain*
[16]*Fermi National Accelerator Laboratory, P. O. Box 500, Batavia, Illinois 60510, USA*
[17]*Physics Department, William Jewell College, Liberty, Missouri 64068, USA*
[18]*SLAC National Accelerator Laboratory, Menlo Park, California 94025, USA*
[19]*University Observatory, LMU Faculty of Physics, Scheinerstrasse 1, 81679 Munich, Germany*
[20]*Ruhr University Bochum, Faculty of Physics and Astronomy, Astronomical Institute, German Centre for Cosmological Lensing, 44780 Bochum, Germany*
[21]*Centro de Investigaciones Energéticas, Medioambientales y Tecnológicas (CIEMAT), Madrid, Spain*
[22]*Nordita, KTH Royal Institute of Technology and Stockholm University, Hannes Alfvéns väg 12, SE-10691 Stockholm, Sweden*
[23]*Instituto de Física Teórica UAM/CSIC, Universidad Autónoma de Madrid, 28049 Madrid, Spain*
[24]*Laboratoire de Physique des 2 Infinis Irène Joliot-Curie, CNRS Université Paris-Saclay, Bátiment 100, F-91405 Orsay Cedex, France*
[25]*Departament de Física, Universitat Autònoma de Barcelona (UAB), 08193 Bellaterra (Barcelona), Spain*
[26]*Kavli Institute for Particle Astrophysics and Cosmology, P. O. Box 2450, Stanford University, Stanford, California 94305, USA*
[27]*Department of Physics, Stanford University, 382 Via Pueblo Mall, Stanford, California 94305, USA*

[28]Physik-Institut, University of Zürich, Winterthurerstrasse 190, CH-8057 Zürich, Switzerland
[29]Cerro Tololo Inter-American Observatory, NSF's National Optical-Infrared Astronomy Research Laboratory, Casilla 603, La Serena, Chile
[30]Laboratório Interinstitucional de e-Astronomia—LIneA, Avenida Pastor Martin Luther King Jr., 126 Del Castilho, Nova América Offices, Torre 3000/sala 817 CEP: 20765-000, Brazil
[31]INAF-Osservatorio Astronomico di Trieste, via G. B. Tiepolo 11, I-34143 Trieste, Italy
[32]Department of Physics, University of Michigan, Ann Arbor, Michigan 48109, USA
[33]Institute of Cosmology and Gravitation, University of Portsmouth, Portsmouth, PO1 3FX, United Kingdom
[34]Department of Physics, Northeastern University, Boston, Massachusetts 02115, USA
[35]Department of Physics and Astronomy, University College London, Gower Street, London, WC1E 6BT, United Kingdom
[36]School of Mathematics and Physics, University of Queensland, Brisbane, Queensland 4072, Australia
[37]Universidad de La Laguna, Departamento Astrofísica, E-38206 La Laguna, Tenerife, Spain
[38]Instituto de Astrofisica de Canarias, E-38205 La Laguna, Tenerife, Spain
[39]Center for Astrophysical Surveys, National Center for Supercomputing Applications, 1205 West Clark Street, Urbana, Illinois 61801, USA
[40]Department of Astronomy, University of Illinois at Urbana-Champaign, 1002 West Green Street, Urbana, Illinois 61801, USA
[41]Hamburger Sternwarte, Universität Hamburg, Gojenbergsweg 112, 21029 Hamburg, Germany
[42]Department of Physics, IIT Hyderabad, Kandi, Telangana 502285, India
[43]Université Grenoble Alpes, CNRS, LPSC-IN2P3, 38000 Grenoble, France
[44]Department of Astronomy/Steward Observatory, University of Arizona, 933 North Cherry Avenue, Tucson, Arizona 85721-0065, USA
[45]Jet Propulsion Laboratory, California Institute of Technology, 4800 Oak Grove Drive, Pasadena, California 91109, USA
[46]Department of Physics and Astronomy, University of Waterloo, 200 University Avenue West, Waterloo, Ontario N2L 3G1, Canada
[47]California Institute of Technology, 1200 East California Boulevard, MC 249-17, Pasadena, California 91125, USA
[48]Instituto de Fisica Teorica UAM/CSIC, Universidad Autonoma de Madrid, 28049 Madrid, Spain
[49]Department of Physics and Astronomy, Pevensey Building, University of Sussex, Brighton, BN1 9QH, United Kingdom
[50]Santa Cruz Institute for Particle Physics, Santa Cruz, California 95064, USA
[51]Department of Physics, The Ohio State University, Columbus, Ohio 43210, USA
[52]Center for Cosmology and Astro-Particle Physics, The Ohio State University, Columbus, Ohio 43210, USA
[53]Center for Astrophysics | Harvard & Smithsonian, 60 Garden Street, Cambridge, Massachusetts 02138, USA
[54]Australian Astronomical Optics, Macquarie University, North Ryde, New South Wales 2113, Australia
[55]Lowell Observatory, 1400 Mars Hill Road, Flagstaff, Arizona 86001, USA
[56]George P. and Cynthia Woods Mitchell Institute for Fundamental Physics and Astronomy, and Department of Physics and Astronomy, Texas A&M University, College Station, Texas 77843, USA
[57]Institució Catalana de Recerca i Estudis Avançats, E-08010 Barcelona, Spain
[58]Department of Physics, University of Cincinnati, Cincinnati, Ohio 45221, USA
[59]Perimeter Institute for Theoretical Physics, 31 Caroline Street North, Waterloo, Ontario N2L 2Y5, Canada
[60]Centro de Tecnologia da Informação Renato Archer, Campinas, SP, 13069-901, Brazil
[61]Observatório Nacional, Rio de Janeiro, RJ, 20921-400, Brazil
[62]Department of Physics, Carnegie Mellon University, Pittsburgh, Pennsylvania 15312, USA
[63]Department of Physics, University of Genova and INFN, Via Dodecaneso 33, 16146, Genova, Italy
[64]Brookhaven National Laboratory, Building 510, Upton, New York 11973, USA
[65]Department of Physics and Astronomy, Stony Brook University, Stony Brook, New York 11794, USA
[66]Physics Department, Lancaster University, Lancaster, LA1 4YB, United Kingdom

[67]Computer Science and Mathematics Division, Oak Ridge National Laboratory, Oak Ridge, Tennessee 37831, USA

(Received 10 November 2025; accepted 18 February 2026; published 26 June 2026)

This work is part of a series establishing the redshift framework for the 3×2pt analysis of the Dark Energy Survey Year 6 (DES Y6). For DES Y6, photometric redshift distributions are estimated using self-organizing maps (SOMs), calibrated with spectroscopic and many-band photometric data. To overcome limitations from color-redshift degeneracies and incomplete spectroscopic coverage, we enhance this approach by incorporating clustering-based redshift constraints (clustering-z, or WZ) from angular cross-correlations with BOSS and eBOSS galaxies and eBOSS quasar samples. We define a WZ likelihood and apply importance sampling to a large ensemble of SOM-derived $n(z)$ realizations, selecting those consistent with the clustering measurements to produce a posterior sample for each lens and source bin. The analysis uses angular scales corresponding to 1.5–5 Mpc to optimize signal-to-noise ratio while mitigating modeling uncertainties and marginalizes over redshift-dependent galaxy bias and other systematics informed by the N-body simulation CARDINAL. While a sparser spectroscopic reference sample limits WZ constraining power at $z > 1.1$, particularly for source bins, we demonstrate that combining SOM with WZ improves redshift accuracy and enhances the overall cosmological constraining power of DES Y6. We estimate an improvement in S_8 of approximately 10% for cosmic shear and 3×2pt analysis, primarily due to the WZ calibration of the source samples.

DOI: 10.1103/6lfl-h6dg

I. INTRODUCTION

Accurately determining the redshift distributions $n(z)$ of lens and source galaxy samples is crucial for correct interpretation of cosmological measurements of galaxy clustering and weak gravitational lensing (see, e.g., [1–4]). The cost in time and money obtaining spectroscopic redshifts for every galaxy is impractical for the $> 100 \times 10^6$ galaxies in present-day imaging surveys such as the Dark Energy Survey (DES). "Photometric redshifts" (photo-z's, or PZ) can be estimated from multiband photometry of each galaxy. A wide range of photo-z methods exist (e.g., [5–8]). The approach adapted by DES and other surveys [9–13] partitions the photometric space with self-organizing maps (SOMs) and calibrates each SOM "cell" with spectroscopic and/or many-band photometric redshifts, which enables careful quantification of various sources of uncertainty. This framework is referred as SOMPZ (SOM+PZ). Photometric methods are, however, inherently limited by color-redshift degeneracies and by the lack of fully representative spectroscopic samples for both training and calibration [12,14].

Clustering-based redshift estimation [WZ, where W refers to $w(\theta)$] provides a complementary method for constraining redshift distributions (see, e.g., [2,15–25]). Unlike photometric methods, clustering-based redshift techniques are not affected by photometric noise, the large statistical uncertainties from small deep fields, or the need for fully representative spectroscopic samples. Instead, they rely on angular cross-correlations between the photometric samples and auxiliary spectroscopic samples with secure redshifts. When two samples overlap in redshift, they trace the same underlying dark matter field, leading to a measurable angular correlation. The amplitude of this correlation thus provides information on the redshift distribution of the photometric sample. This amplitude is, however, degenerate with the biases of both galaxy samples with respect to the dark matter, making galaxy-bias estimation a crucial step [10,15–18,24–26]. The bias of the spectroscopic sample, with its known $n(z)$, can be directly inferred from its autocorrelation functions for a known cosmology. But estimating the bias of the photometric sample, with unknown $n(z)$, is more challenging.

Since both PZ and WZ approaches to measuring $n(z)$ have their respective strengths and weaknesses, for the analysis of the full 6-year DES catalogs (DES Y6), we combine both types of information to estimate the necessary $n(z)$ functions and their uncertainties. Figure 1 is a visual summary of the steps in generating the probability distributions of the DES Y6 galaxy samples' $n(z)$ functions.

This article is one of four papers that describe the redshift treatment for the DES Y6 "3×2pt" analysis of angular correlations among weak-lensing and galaxy-density fields: (1) Yin *et al.* [27] describe the derivation of the SOMPZ redshift estimates for the source galaxy sample; (2) Giannini *et al.* [28] describe the derivation of the SOMPZ redshift estimates for the lens galaxy sample; (3) this article describes how the clustering information is incorporated into the redshift estimates; and (4) Bernstein *et al.* [29] describe a novel approach to sample over the redshift uncertainty during the cosmological inference. Together, the four papers coherently describe the Y6

*Contact author: wdoumerg@ifae.es

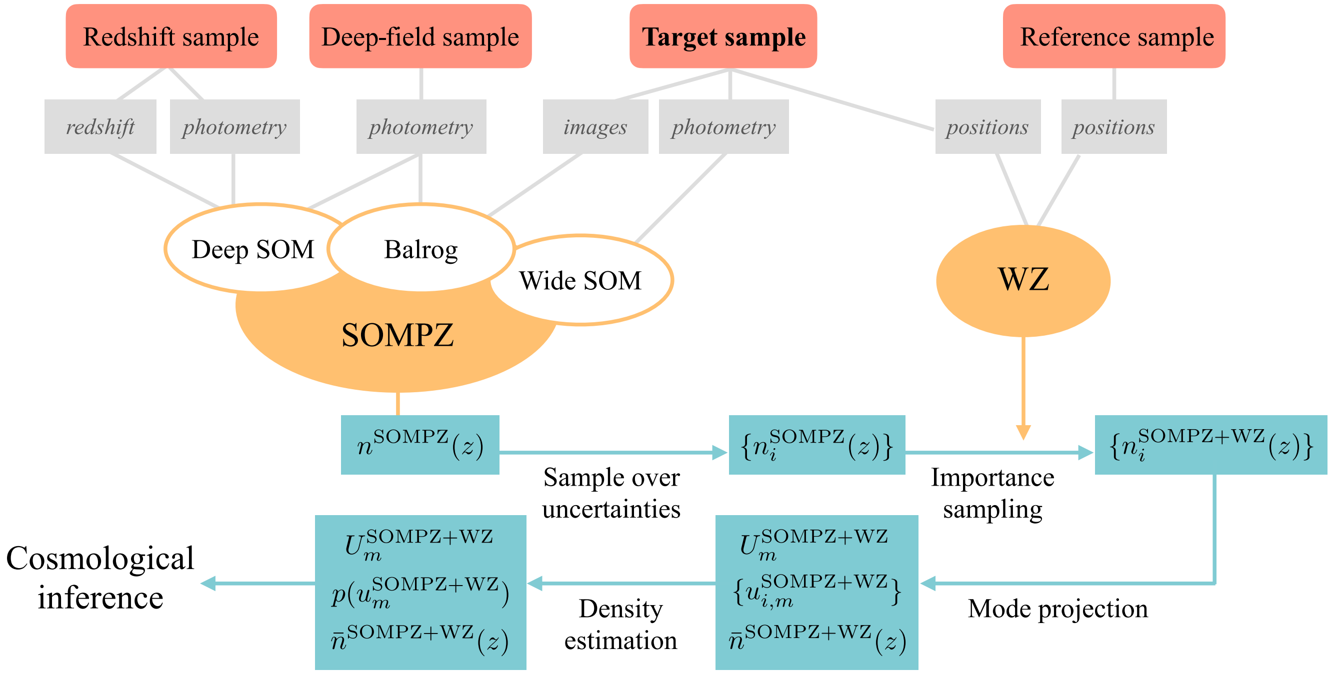

FIG. 1. Flowchart summarizing the DES Y6 3×2pt redshift calibration pipeline. Photometric data for targeted subsets of the DES Y6 galaxy catalog are placed into SOMs, with the redshift distributions of each SOM cell estimated from better-observed galaxies in DES deep fields, along with an observational "transfer function" from deep to wide observational properties derived from the "Balrog" source injection simulations. Sampling over the associated uncertainties produces a set of realizations, $n_i^{\mathrm{SOMPZ}}(z)$. The constraints on $n(z)$ implied by clustering information (WZ), described in this work, are realized by importance sampling the $n_i^{\mathrm{SOMPZ}}(z)$ to yield $n_i^{\mathrm{SOMPZ+WZ}}(z)$ realizations. These are then projected onto a small number of modes that capture all of the cosmologically relevant variation, enabling a more accurate marginalization over the redshift distribution in cosmological inference. Note that for weak-lensing source galaxies, there is an additional step of correction for image blending, applied after the mode projection. Yin *et al.* [27] and Giannini *et al.* [28] contain longer descriptions of the full redshift pipeline.

redshift estimate pipeline. In addition, two related papers play a crucial role in our analysis: (a) Mau *et al.* [30] describe the source redshift correction due to blending; and (b) Giannini *et al.* [31] describe the shear ratio validation for the lens and source redshift.

In this work, we follow the approach to uncertainties in galaxy biases (and other WZ theory and measurement systematic errors) used for DES Year 3 (DES Y3) analyses by Giannini *et al.* [10,17]. N-body simulated catalogs are used to define priors for the photometric galaxies' bias and its redshift evolution, as well as other clustering-related systematics. These redshift-dependent systematics are marginalized over in the calibration.

The amplitude of angular clustering, along with its signal-to-noise ratio (SNR), depends on the scale range considered. In earlier studies, very small scales (0.1–1.5 Mpc) were commonly used [15,16,19,26,32]. These scales offer high-SNR data vectors and are not used for cosmological analyses, ensuring a degree of independence between calibration and cosmological inference. In DES Y3, a larger-scale range (1.5–5 Mpc) was adopted, as it still provided a good SNR while being less affected by nonlinearities and 1-halo physics, and remained separate from the scales used in cosmological analyses [10,17]. More recently, d'Assignies *et al.* [24] tested various scale ranges using state-of-the-art mocks and found 1.5–5 Mpc to be optimal. Based on these findings, we adopt this scale range as the default in this work, while also exploring alternative ranges with our data.

The precision of WZ estimation depends on the redshift and sky overlap between the photometric and the spectroscopic data. In this work, we use spectroscopic data from the BOSS and eBOSS surveys [33,34], which unfortunately overlap only 700–800 deg^2 of the $\approx$5000 deg^2 of the DES Y6 footprint. Furthermore, the dense samples from BOSS and eBOSS surveys only cover the $0 < z < 1.1$ range, whereas our DES catalogs extend to $z_{\mathrm{p}} = 2$. Thus in this work we additionally use the eBOSS Quasi Stellar Object (QSO) sample to extend WZ up to $z = 2.2$ to constrain the DES sources bins, but with limited constraining power due to its sparser space density. Unlike DES Y3 WZ, we do not use Redmagic [17,35] as a reference sample to calibrate the sources $n(z)$, because the systematic uncertainties arising from its photometric selection and redshift assignment are found to negate any statistical gains from its inclusion.

The denser and larger DESI DR1 data [36] became available in March 2025, too late for inclusion in the DES

Y6 3×2 analysis, but a quick examination (also presented in this article) suggests that the DESI DR1 cross-correlations with DES Y6 catalogs are fully consistent with the BOSS/eBOSS values. Future analyses of DES Y6 that would benefit from more accurate $n(z)$ characterization than given here should include DES × DESI clustering.

The paper is structured as follows. In Sec. II we describe the WZ methodology we have adopted to estimate and calibrate the redshift distribution of the MagLim galaxy samples used as the WL lens population and as density tracers, as well as the Metadetect galaxy samples that form the weak lensing (WL) source populations. In Sec. III we describe the data used in this work, including DES data as well as external spectroscopic catalogs. We present the results of our calibration in Sec. IV and examine the impact of the WZ information on cosmological results. Finally, we conclude in Sec. V.

II. METHODOLOGY

In this section, we describe the WZ methodology. In Sec. II A we introduce the modeling of angular clustering, magnification, and clustering redshifts systematics. In Sec. II B we briefly present how we measure in practice the different correlations and covariance from the data. Finally in Sec. II C we explain how the constraints on the redshift distributions are extracted from the data measurements.

A. Modeling of the angular clustering

The WZ method can be summarized as follows.

(i) We have one or more unknown samples u, each of which has a redshift distribution $n_{\mathrm{u}}(z)$ that we wish to determine.

(ii) We have multiple reference samples r_i, each with a secure redshift distribution $n_{\mathrm{r}_i}(z)$. In this article, we will use spectroscopic samples.

(iii) The intrinsic cross-correlation between two samples is nonzero only for pairs of objects in close proximity in z, in which case they trace the same matter field. This intrinsic signal is contaminated with an apparent angular clustering caused by gravitational lensing magnification.

(iv) We evaluate cross-correlations of u and $\{\mathrm{r}_i\}$, where the latter are the spectroscopic samples binned into small spectroscopic slices $z_i \pm \Delta z/2$. The amplitudes of the cross-correlations inform $n_{\mathrm{u}}(z_i)$.

We now detail the modeling of the measured cross-correlations.

1. Galaxy clustering

We use similar conventions to Krause *et al.* [37] for the two-point statistics. One change relative to previous clustering redshifts works (e.g., [17,24]) is that the unknowns' distributions $n_{\mathrm{u}}(z)$ are expressed as sums over a set of basis functions $K_j(z)$ rather than assuming top-hat bins [cf. Eq. (7)], which allows for the inclusion of additional clustering effects. It also improves numerical evaluations of the different WZ elements (in particular the likelihood). The underlying model for the density $\rho_x \propto \mathrm{d}^3N/\mathrm{d}z\mathrm{d}^2\theta$ at redshift z along line of sight θ for members of a galaxy selection x is

$$\rho_x(z,\theta) = n_x(z)(1 + B_x[z, \delta_{\mathrm{m}}(z,\theta)])[1 + \alpha_x \mu(z,\theta)], \quad (1)$$

where δ_{m} is the overdensity of mass at the location (z,θ); B_x is some biasing function for the galaxies in x, which could depend on redshift; $\mu(z,\theta)$ is the gravitational lensing magnification imposed by the foreground line of sight to z, θ; and α_x is the magnification coefficient for the galaxies in x. Any correlations between $\delta_{\mathrm{m}}(z,\theta)$ and $\mu(z,\theta)$ are weak enough to ignore [38,39].

Integrated angular clustering correlation. Let x and y refer to two galaxy samples, with $x = y$ referring to the autocorrelation. We choose a weighting function[1] $W(\theta)$ to convert the angular cross-clustering $w_{xy}(\theta)$ of the two samples to a scalar value w_{xy}, which can be written as

$$w_{xy} = \int \mathrm{d}\theta W(\theta) \sum_{\ell} \frac{2\ell+1}{4\pi} C^{xy}_{\mathrm{gg}}(\ell) \mathcal{L}_\ell(\cos\theta) + w^{\mu}_{xy}, \quad (2)$$

where $C^{xy}_{\mathrm{gg}}(\ell)$ is the angular cross-power power spectrum between the projected intrinsic (unlensed) densities of x and y, $\mathcal{L}_\ell$ is the Legendre polynomial of order ℓ, and w^{μ}_{xy} is the contribution from lensing magnification (which we derive below). The angular clustering power spectrum can be expressed as

$$\begin{aligned} C^{xy}_{\mathrm{gg}}(\ell) &= \int \mathrm{d}\chi \frac{\mathcal{W}^x_{\mathrm{g}} \mathcal{W}^y_{\mathrm{g}}}{\chi^2} P_{xy}\left(k = \frac{\ell + 0.5}{\chi}, z(\chi)\right) \\ &= \int \mathrm{d}z n_x(z) n_y(z) b_x(z) b_y(z) \frac{H(z)}{c\chi^2} P_{\mathrm{m}}(k(\ell,\chi), z), \end{aligned} \quad (3)$$

where $\mathcal{W}^x_{\mathrm{g}} = n_x(z) \frac{\mathrm{d}z}{\mathrm{d}\chi}$ is the normalized selection function, and P_{xy} and P_{m} are the 3D galaxy cross-spectra and (nonlinear) matter power spectra, respectively. The second line assumes that the biasing functional is linear, $b_x(z,\delta_{\mathrm{m}}) = b_x(z)\delta_{\mathrm{m}}$, for both samples, as is typically assumed for the WZ method [16,17,19,22,25,26,32]. The nonlinear power spectrum is numerically evaluated with the default configuration of the CCL library[2] [40], which is based on predictions from CLASS [41] and HALOFIT [42]. Departures from linear bias are a potential source of systematic errors in this model, which we allow for as

[1]In this work we use a power law $W(\theta) = \theta^{-1}/\int \mathrm{d}\theta\theta^{-1}$ [24].
[2]https://github.com/LSSTDESC/CCL

described below. For a longer discussion about the validity of this assumption, we refer to d'Assignies *et al.* [24].[3] The result of this latter article[4] is that the assumption of linear bias with nonlinear power spectrum is good enough for scales down to 1.5 Mpc. In our context of redshift calibration, we are not trying to extract small-scale cosmological information, merely using the fluctuations as indicators of physical proximity. In later sections of this work, we perform additional tests on the Y6 data to test this claim.

We introduce the projected matter correlation function

$$w_{\mathrm{m}}(z) = \frac{H(z)}{c\chi^2}\int \mathrm{d}\theta W(\theta) \times \sum_{\ell} \frac{2\ell+1}{4\pi} P_{\mathrm{m}}(k(\ell,\chi),z)\mathcal{L}_{\ell}(\cos\theta), \quad (4)$$

and rewrite the galaxy-integrated angular correlation as

$$w_{xy} = \int \mathrm{d}z b_x(z) b_y(z) n_x(z) n_y(z) w_{\mathrm{m}}(z) + w^{\mu}_{xy}. \quad (5)$$

Autocorrelation of the reference. For clustering redshifts, we need to measure the galaxy bias of each of the reference samples r_i. We neglect the redshift evolution of b_{r_i} in Eq. (5) as the reference samples are binned in narrow redshift ranges. We neglect as well the lensing magnification, which is nonzero only for galaxy pairs at well-separated redshifts. Thus the galaxy bias is

$$b_{\mathrm{r}_i} = \sqrt{\frac{w_{\mathrm{r}_i\mathrm{r}_i}}{\int \mathrm{d}z n^2_{\mathrm{r}_i}(z) w_{\mathrm{m}}(z)}}. \quad (6)$$

As a consequence, if n_{r_i} is known (which is the case for spectroscopic samples), we can use the measurements $w_{\mathrm{r}_i\mathrm{r}_i}$ to infer the values b_{r_i} of the reference galaxies' biases.

Cross-correlation. We want to extract information on the redshift distribution of the unknown sample $n_{\mathrm{u}}(z)$ by cross-correlating it with many reference samples r_i. First, we decompose the unknown redshift distribution over a basis,

$$n_{\mathrm{u}}(z) = \sum_j f^j_{\mathrm{u}} K_j(z), \quad (7)$$

with $K_j(z)$ the basis, and f^j_{u} the coefficients of the decomposition. We use sawtooth functions, as they naturally give $n(z) \to 0$ as $z \to 0$ and are continuous,

$$K_j(z) = \frac{1}{\Delta z}\Lambda\left(\frac{z}{\Delta z} - j\right),$$
$$\text{with} \quad \Lambda(a) = \begin{cases} a, & 0 < a < 1 \\ 2-a, & 1 < a < 2 \\ 0, & \text{otherwise.} \end{cases} \quad (8)$$

The modeling of the cross-correlation reduces to

$$\begin{aligned} w_{\mathrm{ur}_i} &= b_{\mathrm{r}_i}\int \mathrm{d}z \sum_j b_{\mathrm{u}_j} f^j_{\mathrm{u}} K_j(z) n_{\mathrm{r}_i}(z) w_{\mathrm{m}}(z) + w^{\mu}_{\mathrm{ur}_i} \\ &= \sum_j b_{\mathrm{u}_j} f^j_{\mathrm{u}} A_{ji} + w^{\mu}_{\mathrm{ur}_i} \end{aligned} \quad (9)$$

where we assume the galaxy bias of the unknown sample is a constant b_{u_j} over the support of each element j of the basis and where

$$A_{ji} = b_{\mathrm{r}_i}\int \mathrm{d}z K_j(z) n_{\mathrm{r}_i}(z) w_{\mathrm{m}}(z). \quad (10)$$

2. Magnification

The angular correlation of x and y, caused by magnification is, at first order,

$$w^{\mu}_{xy} = \int \mathrm{d}\theta W(\theta) \sum_{ij\in\{\mathrm{g}\mu,\mu\mathrm{g}\}} c^i_x c^j_y \int \mathrm{d}\chi \frac{\mathcal{W}^x_i \mathcal{W}^y_j}{\chi^2} \times \sum_{\ell}\frac{2\ell+1}{4\pi}\mathcal{L}_{\ell}(\cos\theta) P_{\mathrm{m}}(k(\ell,\chi),z(\chi)), \quad (11)$$

where $c^{\mathrm{g}}_x = b_x$ is the galaxy bias, $c^{\mu}_x = \alpha_x$ is the magnification coefficient,[5] and $\mathcal{W}_{\mu}$ is the lensing efficiency,

$$\mathcal{W}^x_{\mu} = \frac{3\Omega_{\mathrm{m}} H_0^2}{2c^2}\int_{\chi}^{\infty} \mathrm{d}\chi' n_x(\chi') \frac{\chi}{a(\chi)} \frac{\chi'-\chi}{\chi'}. \quad (12)$$

Reordering the terms, and using the integrated matter correlation w_{m} from Eq. (4), we have

[3] We refer to Sec. III A 3 for a discussion on linear treatment of galaxy bias with nonlinear matter power spectrum modeling and its estimation, Appendix B where the relation between galaxy and matter field is treated at second order, and propagated to the modeling of the observables, and Sec. IV C for a measurement of the linear galaxy bias at different scales.

[4] d'Assignies *et al.* [24] uses mocks from Euclid Flagship 2 simulation [43] and the same numerical power spectrum as in the current work.

[5] Please note there is a large variety of notations in the literature, often in conflict. E.g., what we refer to as α is often written $2(\alpha - 1)$, e.g., in Hildebrandt [44], $(C_{\mathrm{sample}} - C_{\mathrm{area}})/2$, e.g., in Elvin-Poole *et al.* [38].

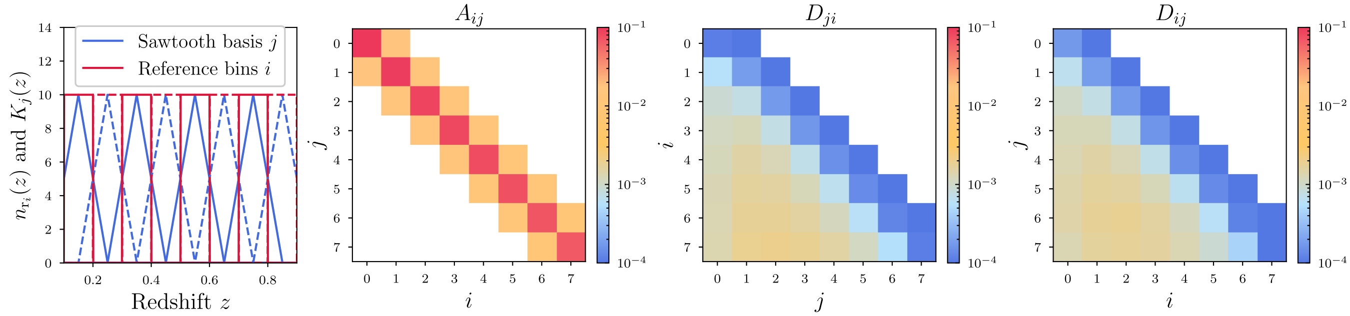

FIG. 2. Illustration of the clustering and magnification for eight sawtooth distributions (on the left panel odd j are represented by solid lines and even with dashed) cross-correlated with eight rectangle reference bins, both with $\Delta z = 0.1$. Clustering matrix A and magnification matrices D are then 8×8. The orange values are 1 order of magnitude smaller than the red, and the blue, 2 orders of magnitude. Matrix coefficients in white are exactly 0. Please note that $D_{\mathrm{r}_i j}$ and $D_{j\mathrm{r}_i}$ are very similar but not exactly equal because for this calculation we have taken similar Δz binning but with sawtooth kernels for the unknowns u and rectangular (boxcar) kernels for the references r.

$$w^{\mu}_{xy} = \frac{3\Omega_{\mathrm{m}} H_0}{c} \int_0^{\infty} \mathrm{d}z b_x(z) n_x(z) \frac{H_0(1+z)}{H(z)} w_{\mathrm{m}}(z) \times \int_z^{\infty} \mathrm{d}z' \alpha_y(z') n_y(z') \frac{\chi(z') - \chi(z)}{\chi(z')} \chi(z) + \{x \leftrightarrow y\}, \tag{13}$$

where $\{x \leftrightarrow y\}$ represents the same term, but switching the x and y indices. Decomposing the u distribution over the K_j basis, the two magnification terms can be very compactly written

$$w^{\mu}_{\mathrm{ur}_i} = \sum_j f^j_{\mathrm{u}} [b_{\mathrm{u}_j} \alpha_{\mathrm{r}_i} D_{ji} + b_{\mathrm{r}_i} \alpha_{\mathrm{u}_j} D_{ij}], \tag{14}$$

where we introduce the D_{ij} matrices, independent of any b or μ values, that capture the amplitude of the magnification μ of galaxies in kernel j by the matter in kernel i,

$$D_{ij} = \frac{3\Omega_{\mathrm{m}} H_0}{c} \int_0^{\infty} \mathrm{d}z_i K_i(z_i) \frac{H_0(1+z_i)}{H(z_i)} w_{\mathrm{m}}(z_i) \times \int_{z_i}^{\infty} \mathrm{d}z_j K_j(z_j) \frac{\chi(z_j) - \chi(z_i)}{\chi(z_j)} \chi(z_i). \tag{15}$$

In this formula we have assumed that $n_{\mathrm{r}_i}(z) = K_i(z)$, but one is free to reintroduce the explicitly known value of $n_{\mathrm{r}_i}(z)$ under the appropriate integral—this will not make much difference, as can be seen by comparing the two rightmost panels of Fig. 2, which swap the rectangular n_{r_i} bins for the different appearances of the kernel K_i in this equation for D_{ij}. The final theoretical expression for the cross-correlation is then

$$w_{\mathrm{ur}_i} = \sum_j f^j_{\mathrm{u}} [b_{\mathrm{u}_j} A_{ji} + \alpha_{\mathrm{u}_j} b_{\mathrm{r}_i} D_{ij} + b_{\mathrm{u}_j} \alpha_{\mathrm{r}_i} D_{ji}]. \tag{16}$$

In Fig. 2 we show the clustering and magnification matrices for a set of eight reference rectangular bins and eight sawtooth bins, playing the role of the basis K_j. The clustering matrix is mainly diagonal, as expected. The magnification matrices D are lower triangular because for tracers in bin j to be magnified by the matter in i, the latter has to be localized at lower redshift. We also see that the amplitude of magnification is 1 order of magnitude smaller than the clustering, but couples more bin pairs.

3. Systematic errors

The model used to derive Eq. (16) is incomplete in known respects, most importantly that the linear-bias model does not hold precisely, especially at smaller separations, and we will fit models in which $b_{\mathrm{u}}, \alpha_{\mathrm{u}}, b_{\mathrm{r}}$, and α_{r} are constant across redshift z. There may be other systematic errors as well, which we will detail later. When fitting the data to this model, we will therefore introduce a "systematic-error" function S into the model for the intrinsic-clustering term, as in Gatti *et al.* [17]. The magnification terms are smaller corrections to the intrinsic-clustering term, so that any deviation from our magnification modeling can be easily absorbed into the bias on intrinsic clustering,

$$\hat{w}_{\mathrm{ur}_i} = \sum_j f^j_{\mathrm{u}} [b_{\mathrm{u}_j} A_{j\mathrm{r}_i} (1 + S_{\mathrm{ur}_i}) + \alpha_{\mathrm{u}_j} b_{\mathrm{r}_i} D_{ij} + b_{\mathrm{u}_j} \alpha_{\mathrm{r}_i} D_{ji}]. \tag{17}$$

The S function is chosen to be a function of z whose scale and amplitude of variability can be "dialed in" to match the level that the model Eq. (16) departs from the true w_{ur} values in simulations. We choose

$$S_{\mathrm{ur}_i} = \sum_{k=0}^{M} s_{\mathrm{u}k} \frac{\sqrt{2k+1}}{0.85} \mathcal{L}_k(\tilde{z}) \quad \text{with} \quad \tilde{z} \equiv 0.85 \times \frac{2z - z_{\max} - z_{\min}}{z_{\max} - z_{\min}}. \tag{18}$$

$\tilde{z}$ is a linear remapping of z from the range $[z_{\min}, z_{\max}]$ to $[-0.85, 0.85]$. The maximum degree M of the Legendre polynomials $\mathcal{L}_k$ controls how rapidly $S(z)$ can vary across its range. Gaussian priors on the $s_{\mathrm{u}k}$ coefficients control the (scale-dependent) amplitude of the deviations of the model from the simple linear-bias model. The fit of the model in Eq. (17) to the data is done with the $\{s_{\mathrm{u}k}\}$ allowed to vary. The choices of the order M and the priors $\sigma(s_{\mathrm{u}k})$ are made by examining the deviation between the "observed" w_{ur} and the model in Eq. (16) in the CARDINAL simulations of the DES Y6 catalogs [45]. This process is described in Sec. IV A.

We have the option of parametrizing multiple uncorrelated systematic errors independently in the same Legendre basis, with prior width amplitudes $s_{q\mathrm{u}k}$ for systematic errors indexed by q. Then, when calculating likelihoods for the data, we can combine the multiple systematic errors' effects by $\sigma^2(s_{\mathrm{u}k}) = \sum_q \sigma^2(s_{q\mathrm{u}k})$.

B. Measurement of the cross-correlations and their uncertainties

In this section, we describe the methods for obtaining estimates of and uncertainties on the observables $\hat{w}_{\mathrm{ur}}$ and $\hat{w}_{\mathrm{rr}}$ from the catalogs of DES Y6 galaxies and the spectroscopic catalogs.

1. Data estimator and scale weighting

We use the Davis and Peebles (DP) [46] or the Landy-Szalay (LS) [47] estimator, depending upon whether a simulated catalog of random (unclustered) position sample is available for the unknown data. The estimators for the integrated correlation functions are

$$w_{xy}^{\mathrm{DP}} \approx \sum_i \Delta\theta_i W(\theta_i) \frac{\mathrm{D}_x\mathrm{D}_y(\theta_i) - \mathrm{R}_x\mathrm{D}_y(\theta_i)}{\mathrm{R}_x\mathrm{D}_y(\theta_i)}, \tag{19}$$

$$w_{xy}^{\mathrm{LS}} \approx \sum_i \Delta\theta_i W(\theta_i) \frac{(\mathrm{D}_x - \mathrm{R}_x)(\mathrm{D}_y - \mathrm{R}_y)(\theta_i)}{\mathrm{R}_x\mathrm{R}_y(\theta_i)}, \tag{20}$$

where $XY(\theta_i)$ are counts of pairs of catalog members with separations in a bin centered at θ_i with width $\Delta\theta_i$, and $X, Y \in \{D, R\}$ are counts of the data or random catalogs. We use ten logarithmically spaced bins between the angles corresponding to comoving transverse scales r_{p} of 1.5–5 Mpc, with $W(\theta) = \theta^{-1} / \sum_i \Delta\theta_i\theta_i^{-1}$. These estimators are evaluated with TreeCorr [48], a highly efficient, open-source, user-friendly Python package.

2. Covariance

We estimate the covariance matrix C_w of the w_{ur_i} values with the jackknife method, splitting the overlap of the DES Y6 footprint with the BOSS footprint into 100 subregions to capture both shot noise and sample variance.[6] Inverses of jackknife covariances are corrected for finite sampling as per Hartlap *et al.* [49]. Because the spectroscopic reference sample's bins r_i and r_j have no overlap in redshift for $i \neq j$, we expect $\mathrm{Cov}(w_{\mathrm{ur}_i}, w_{\mathrm{ur}_j})$ to be near zero. This is found to be true to within measurement error both for data and in the much larger area of the CARDINAL simulated data and was also tested with numerical estimates of the covariance. We therefore set to zero all such terms. As the noise from finite number of patches is greatly suppressed by this procedure, we do not apply Hartlap corrections when inverting these covariances. Comparison of the Hartlap-corrected inverse of the noisy covariance to the inverse of this "cleaned" covariance yielded consistent diagonal elements, in both data and CARDINAL (cf. Sec. III).

When there are multiple unknown galaxy samples $N_{\mathrm{u}} > 1$ under study, we also set to zero all the covariances involving two different spectroscopic bins, $\mathrm{Cov}(w_{\mathrm{u}_i,\mathrm{r}_j}, w_{\mathrm{u}_k,\mathrm{r}_\ell})$ for $j \neq \ell$, but we can have nonzero $\mathrm{Cov}(w_{\mathrm{u}_i\mathrm{r}_k}, w_{\mathrm{u}_j\mathrm{r}_k})$. If we create a single vector $\mathbf{w}$ by concatenating the w_{ur_i} values for all samples u, the covariance matrix C_w for this vector is block diagonal, with an $N_{\mathrm{u}} \times N_{\mathrm{u}}$ block for each reference sample r_k. This greatly accelerates the calculation of likelihoods described below and was tested with simulated and analytical estimates of the covariances for different realistic cases.

C. WZ posterior probability

With the model and measurements for w_{ur} both in hand, we wish to evaluate the probability that any given proposal for the $n_{\mathrm{u}}(z)$ functions could have produced the observed w_{ur} values. In what follows we will use u and r as indices that run over the samples of unknown and reference galaxies, respectively. The proposed $n_{\mathrm{u}}(z)$ functions are specified by a vector $\mathbf{n} \equiv \{f_{\mathrm{u}}^j\}$ of the coefficients of the expansion Eq. (7), and the data by a vector $\mathbf{w} = \{w_{\mathrm{ur}}\}$ with covariance matrix C_w. We have a model $\hat{\mathbf{w}}(\mathbf{n}, \mathbf{q})$ where there are nuisance parameters $\mathbf{q} = \{b_{\mathrm{u}}, \alpha_{\mathrm{u}}, \alpha_{\mathrm{r}}, s_{\mathrm{u}k}\}$ and b_{r}, that appear in the model. We will assume that the b_{r} are known from their autocorrelations via Eq. (6), letting any errors be absorbed into the systematic-error functions specified by the $s_{\mathrm{u}k}$ coefficients.

We will assume that the likelihood function of the measurements is Gaussian, with a mean at $\hat{\mathbf{w}}$ and covariance matrix of C_w. The posterior probability of the observations given the proposed $\mathbf{n}$ then becomes

$$p(\mathbf{w}|\mathbf{n}) \propto \int \mathrm{d}\mathbf{q}\mathcal{L}(\mathbf{w}|\mathbf{n}, \mathbf{q}) p(\mathbf{q}) \tag{21}$$

[6]The physical size of an 8 deg^2 area is much larger than the correlation function scale (~50–100 vs 2 Mpc).

$$
\begin{aligned}
&\propto \int \mathrm{d}\mathbf{q} \exp\left[-(\mathbf{w}-\hat{\mathbf{w}})^T C_w^{-1}(\mathbf{w}-\hat{\mathbf{w}})/2\right] \\
&\times \exp\left[-\left(\alpha_{\mathrm{r}}-\alpha_{\mathrm{r}}^{(0)}\right)^2/2\sigma^2(\alpha_{\mathrm{r}})\right] \\
&\times \prod_{\mathrm{u}} \exp\left[-(\alpha_{\mathrm{u}}-\alpha_{\mathrm{u}}^{(0)})^2/2\sigma^2(\alpha_{\mathrm{u}})\right] \\
&\times \prod_{\mathrm{u},k} \exp\left[-s_{\mathrm{u}k}^2/2\sigma^2(s_{\mathrm{u}k})\right]. \qquad (22)
\end{aligned}
$$

The last line contains the Gaussian priors that we apply to the single value α_{r} that we assign to all reference bins, the α_{u} magnification coefficient for each unknown sample, and the (zero-mean) $s_{\mathrm{u}k}$ systematic coefficients. We take flat priors for the b_{u} values, which are strongly constrained by the WZ data.

Examination of our $\hat{\mathbf{w}}$ model in Eq. (17) reveals that if we divide the nuisance parameters into $\mathbf{b} = \{b_{\mathrm{u}}\}$ and $\mathbf{q}' = \{\alpha_{\mathrm{u}}, \alpha_{\mathrm{r}}, s_{\mathrm{u}k}\}$, then the posterior probability under the integral is an exponentiated quadratic function of $\mathbf{q}'$. This means we can write the integrand as a normal distribution over $\mathbf{q}'$ with a mean $\mathbf{q}'_0$ and a covariance C'_q that are functions of $\mathbf{n}$ and $\mathbf{b}$,

$$
p(\mathbf{w}|\mathbf{n}) \propto \int \mathrm{d}\mathbf{b}\, c(\mathbf{n},\mathbf{b}) \int \mathrm{d}\mathbf{q}' \mathcal{N}[\mathbf{q}'|\mathbf{q}'_0(\mathbf{n},\mathbf{b}), C'_q(\mathbf{n},\mathbf{b})]. \qquad (23)
$$

There is a $\mathbf{b}$-dependent normalization factor $c(\mathbf{n},\mathbf{b})$, and the integration over $\mathbf{q}'$ can then be done analytically, yielding $|2\pi C'_q|^{1/2}$. We opt to replace the marginalization over the b_{u} variables with an evaluation of the maximum of the integrand (i.e., a profile likelihood)—this should still yield a good estimate of the relative compatibility of any $n(z)$ proposal with the WZ observations.[7] This gives

$$
p(\mathbf{w}|\mathbf{n}) \propto \sup_{\mathbf{b}}\{c(\mathbf{n},\mathbf{b})|C'_q(\mathbf{n},\mathbf{b})|^{1/2}\}. \qquad (24)
$$

The maximization over $\mathbf{b}$ is accomplished by a series of Newton iterations, which are enabled by using automatic differentiation to determine the derivatives of the algebraic expressions for $c(\mathbf{n},\mathbf{b})$ and $C'_q(\mathbf{n},\mathbf{b})$ with respect to $\mathbf{b}$.

D. Importance sampling and photometric uncertainty marginalization

For the cosmological analyses of the DES Y6 data, we need to marginalize the probability of cosmological parameters over the uncertainties in the $n(z)$ distributions of four samples of source galaxies for weak gravitational lensing observations ("source bins") and six samples of galaxies used to trace the deflecting matter distributions ("lens bins"). In each case we wish to combine the constraints on $n(z)$ provided by PZ analyses of the sample members with the WZ information quantified with the previous section's posterior, to yield our strongest constraints on $n(z)$. Using Bayes' theorem,

$$
p(\mathbf{n}|\mathrm{PZ},\mathrm{WZ}) \propto p(\mathrm{WZ}|\mathrm{PZ},\mathbf{n})p(\mathbf{n}|\mathrm{PZ}) = p(\mathbf{w}|\mathbf{n})p(\mathbf{n}|\mathrm{PZ}), \qquad (25)
$$

where $p(\mathrm{WZ}|\mathrm{PZ},\mathbf{n}) = p(\mathbf{w}|\mathbf{n})$ because the WZ likelihood does not depend on the photometry, and $p(\mathbf{n}|\mathrm{PZ})$ is the posterior from photometry described in Sec. II E. Thus we sample from the posterior probability $p(\mathbf{n}|\mathrm{PZ},\mathrm{WZ})$ by

(1) using the method described in Sec. II E to create a large number ($\approx 10^8$) of realizations $\mathbf{n}_i$ from $p(\mathbf{n}|\mathrm{PZ})$;
(2) calculating $p(\mathbf{w}|\mathbf{n}_i)$ for each PZ sample $\mathbf{n}_i$ using Eq. (24);
(3) retaining each $\mathbf{n}_i$ sample with probability $\beta \times p(\mathbf{w}|\mathbf{n}_i)/\max_j[p(\mathbf{w}|\mathbf{n}_j)]$, with β chosen so that the number of samples is around 3000 (the minimum number needed to get noiseless modes, cf. [29]). The samples of $\mathbf{n}$ surviving this importance sampling step are drawn from the joint distribution $p(\mathbf{n}|\mathrm{WZ},\mathrm{PZ})$, cf. Eq. (25).
(4) We apply the compression techniques described in Bernstein *et al.* [29] to find an encoding matrix E such that $\{\mathbf{u}_i\} = \{E\mathbf{n}_i\}$ is a much lower-dimensional representation of $n(z)$ for the unknown population under consideration.[8] A density estimator is then used to find a continuous multidimensional probability distribution $p(\mathbf{u})$ that is plausibly the parent distribution for the $\mathbf{u}_i$ samples. The density estimators are described in Bernstein *et al.* [29].
(5) Samples of $n(z)$ for use in the cosmological analysis can now be produced by sampling from $p(\mathbf{u})$, setting $\mathbf{n} = D\mathbf{u}$ with the decoding matrix D found by the modal analysis, then expressing $n(z)$ from the elements of $\mathbf{n}$ using Eq. (7).

There are some differences between the application of the method to the source galaxies and the application to the lens galaxies. The lenses are more straightforward: each of the six bins' $n(z)$ goes through the full WZ process independently. We can do so because the small overlap in redshift between lens bins leaves little covariance between bins' results [50], so $\mathrm{Cov}(w_{\mathrm{u}_i\mathrm{r}}, w_{\mathrm{u}_j\mathrm{r}})$ can be neglected for $i \neq j$. This is verified with both an analytical covariance matrix [generated assuming SOM $n(z)$] and jackknife estimates of the covariance matrix. There are six independent SOMs used for the SOMPZ calibration of each

[7] We expect the b_{u} parameter to be uncorrelated with redshift parameters [since it is an amplitude, and we want normalized $n(z)$]. In the case of Gaussian likelihood with uninformative flat priors, marginalization and profile likelihood are equal up to a numerical factor.

[8] The notation $\mathbf{u}$ for the compressed representation is not related to the index u enumerating the unknown galaxy samples.

bin [28], six independent applications of the importance sampling, and six distinct encoding/decoding matrices. The derived distribution of the compressed $\mathbf{u}$ samples are seen to be significantly non-Gaussian in some of the lens bins. A straightforward "Gaussianizing" transformation $\mathbf{u} \to \tilde{\mathbf{u}}$ yields a set of $\tilde{\mathbf{u}}$ that are consistent with a multivariate normal distribution with identity-matrix covariance. The cosmology inference pipeline thus needs only to sample over these $\tilde{\mathbf{u}}$ variables, with statistically independent priors, in order to implement marginalization over $p(\mathbf{n}|\mathrm{WZ},\mathrm{PZ})$ for the lenses.

For the source population, there are cosmologically significant correlations between the ith PZ sample $n_{\mathrm{u},i}(z)$ for source bin u with $n_{\mathrm{u}',i}(z)$ from a distinct source bin. Our WZ sampling process must conserve these correlations, so we concatenate the $\mathbf{n}_i$ from all four source redshift bins into a single vector, and we multiply together the $p(\mathbf{n}|\mathrm{WZ})$ posteriors for the bins as well when importance sampling. Another issue with the source bins' samples is that the PZ samples are too noisy to generate high values of $p(\mathbf{n}_i|\mathrm{WZ})$, so the importance sampling fails. To remedy this, we use the mode compression method to project away components of $\mathbf{n}_i$ that vary $n(z)$ in ways that do not affect the DES Y6 observables, e.g., rapid variation with z [27]. The denoised $\hat{\mathbf{n}}_i = DE\mathbf{n}_i$ are used to compute the WZ posterior $p(\hat{\mathbf{n}}_i|\mathrm{WZ})$ for importance sampling. The mode compression is then recalculated using only the samples that survive the importance sampling, i.e., are drawn from the joint PZ + WZ probability. An additional difference between the processing of lens and source galaxies is that the $\mathbf{u}_i$ samples for the source galaxies are seen to be consistent with a unit-normal distribution—no Gaussianization is needed.

E. SOMPZ uncertainty

As highlighted in Secs. II C and II D, we work under the assumption that there exists a set of proposal $\{n_i\}$ realizations of the $n(z)$, representing the distribution $p(\mathbf{n}|\mathrm{PZ})$, which is the range of possible $n(z)$ that is allowed by the information that we have from the photometry of galaxies. In this section we summarize the various sources of uncertainty affecting the distributions of $n(z)$ coming from the photometry of Metadetect and MagLim++ galaxies and how we generate the $\{n_i\}$ realizations of $n(z)$. Detailed descriptions are provided in Yin *et al.* [27] and Giannini *et al.* [28], respectively.

The $n(z)$ for MagLim++ and Metadetect galaxies is measured empirically with the SOMPZ methodology [9–11,51–53], which leverages the DES deep fields as a stepping stone between the wide-field galaxy photometry in the target samples and redshift information. The DES deep fields have deeper photometry with additional photometric bands and overlap with many-band redshift surveys outside of DES. To establish the probability distribution of wide-field photometry given deep-field "truth", i.e., the "transfer function," the BALROG software [54] injects simulated galaxies drawn from the DES deep fields into real DES wide-field images. The measured spectroscopic and many-band photometric redshifts of the deep-field galaxies can in this way be transferred to galaxy bins defined using wide-field photometry. This methodology enables control over all known potential sources of uncertainty impacting the $n(z)$ estimates from galaxy photometry.

To model the uncertainty, Yin *et al.* [27] and Giannini *et al.* [28] adopt a methodology similar to Myles *et al.* [52], incorporating updates from Sánchez *et al.* [53]. We account for uncertainty arising from (i) sample variance and shot noise from the finite area covered by the deep fields; (ii) biases in the redshifts assigned to deep-field galaxies lacking spectroscopy and using multiband photometric assignments instead; (iii) uncertainty in the photometric calibration (zero point) of deep-field galaxies (ZP).

To address the statistical uncertainties in item (i) above, we use the approximate 3sDir model (a product of three Dirichlet distributions), first presented in Sánchez *et al.* [11] and then further developed in Myles *et al.* [52]. Mathematically the model describes $p(\{f_{zc}\}|\{N_{zc}\}) \approx 3\mathrm{sDir}$, where N_{zc} are the number counts of galaxies that have been observed to be at redshift bin z and residing in deep SOM cell c, and $\{f_{zc}\}$ are the underlying fractions of the full galaxy population that reside in redshift bin z and cell c. We constrain $\sum_{zc} f_{zc} = 1$ and $0 \leq f_{zc} \leq 1$. We use the SOM algorithm from Sánchez *et al.* [11], which has been further validated by Campos *et al.* [9] for use on DES Y6 weak-lensing samples. The 3sDir samples of $\{f_{zc}\}$ incorporate the expected sample variance and shot noise. Each such sample can be propagated into $n(z)$ functions for the wide bins by using the BALROG transfer function and the observed color distribution of the bin members.

Next the 3sDir process is modified to account for uncertainties in category (ii), namely resulting from biases and errors in the deep fields' photometric redshift catalogs: COSMOS2020 [55], PAUS + COSMOS [56], and PAUSW1 [57]. As described in Yin *et al.* [27] and Giannini *et al.* [28], a parametrized many-band PZ bias function is constrained separately for distinct magnitude/redshift bin combinations. This expands on the DES Y3 assumption of biases scaling as $(1 + z)$ and also takes a more conservative approach for the uncertainty of these systematic redshift biases.

The 3sDir process is also modified for uncertainties in category (iii), namely the uncertainties from the relative zero-point calibration across different deep fields [14]. Essentially we need to model the relative zero-point error between the COSMOS field (which contains most of the redshifts) and the other three deep fields.

In total, there are 24 relative zero-point systematic shifts (8 bands and 3 out of 4 fields) from category (iii), plus several parameters of the redshift systematics in category (ii) for COSMOS2020, PAUS + COSMOS, and PAUSW1, each with a Gaussian prior. We draw 100 samples of possible values of this nuisance-parameter vector using a Latin hypercube method. For each of these 100 samples, we shift the deep fluxes of galaxies with the selected zero-point errors, recalculate their redshift assignments with the selected PZ biases applied, and reassign them to SOM cells to collect new $\{N_{zc}\}$ values. Then, for each of these 100 samples, we generate 1×10^6 $n(z)$ samples using 3sDir and SOMPZ. In total, we generate 100×10^6 $n(z)$ samples for each of the Metadetect and MagLim++ tomographic bins, which have effectively sampled over all three types of PZ uncertainty.

III. DATA AND THEIR SIMULATED COUNTERPART

This section describes the various photometric and spectroscopic catalogs used for DES Y6 WZ. The calibration of the nuisance parameters with simulated data is critical for our method, so we need mocks with properties as similar as possible to the real datasets. We use the CARDINAL simulation [45] for this purpose. The redshift distributions of the data and mocks are reported in Fig. 3.

A. Unknown data

1. Metadetect

The source galaxies we calibrate in this work are from the Y6 Metadetect shape catalog presented in [58]. The catalog consists of 139.6×10^6 galaxies with the number density of 8.87 galaxies per arc min^2 and shape noise of $\sigma_e = 0.29$. Objects are removed based on star and foreground flags from [59], as well as being outliers in properties such as flux and color (see Sec. 4.4 of [58] and Sec. 2 of [27] for more detail). We also remove objects outside of the joint Large Scale Structure (LSS)-shear footprint as described in [60]. The selected Metadetect galaxies are divided into four tomographic bins of increasing mean redshift on the basis of which SOM cell they belong to, and redshift distributions for each bin are generated under the SOM framework [27].

Thanks to the improvements in point spread function (PSF) modeling since DES Y3 described in [61], we are now able to include g-band flux information for robust redshift calibrations. A statistical weight for each Metadetect object is generated as the inverse variance of shear inference from this source (see Sec. 4.5 of [58] for more detail). All DES Y6 shear measurements incorporate this weighting, hence our

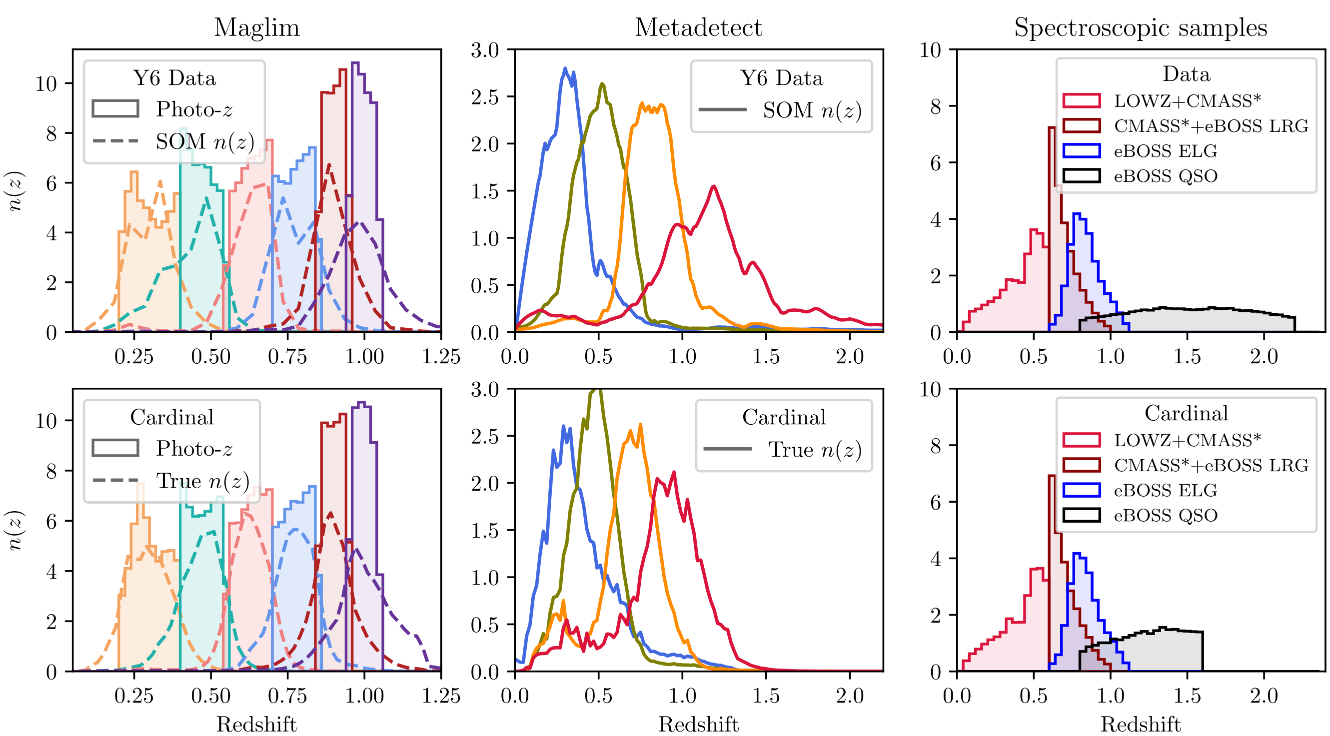

FIG. 3. Redshift distributions of the data (top) and CARDINAL mocks (bottom) are shown for MagLim++ (lenses, left), Metadetect (sources, middle), and BOSS-eBOSS (reference, right). Spectroscopic data are presented as a function of spectroscopic redshift. MagLim++ bins are generated with photo-z cuts, and we plot the photo-z histograms of every bin, along with the corresponding SOM estimate of the $n(z)$ for the data. For Metadetect data, only the SOM estimate of the $n(z)$ is shown. The true redshift distributions are provided for all simulated DES samples. Simulated data do not reproduce properly the $z > 1.5$ distribution of the data.

TABLE I. Summary of the Metadetect sample. For each tomographic bin, we give the (SOM-estimated) mean redshift and redshift width, the number of galaxies, the number density in arc min^{-2}, and the magnification coefficient.

Metadetect	$\langle z\rangle_{\mathrm{SOM}}$	σ_z^{SOM}	N galaxies	n density	α
Bin 1	0.415	0.42	33 707 071	2.555	-0.186 ± 0.022
Bin 2	0.545	0.33	34 580 888	2.252	-0.248 ± 0.026
Bin 3	0.841	0.26	34 646 436	2.368	-0.122 ± 0.024
Bin 4	1.175	0.47	36 727 798	1.694	0.366 ± 0.028

TABLE II. Summary of the MagLim++ sample. For each bin we give the DNF photo-z cuts, the number of galaxies, the number density in arc min^{-2}, and the magnification coefficient.

MagLim++	z range	N galaxies	n density	α
1	$0.20 \le z_{\mathrm{DNF}} < 0.40$	1 852 538	0.128	0.582 ± 0.042
2	$0.40 \le z_{\mathrm{DNF}} < 0.55$	1 335 294	0.092	0.380 ± 0.105
3	$0.55 \le z_{\mathrm{DNF}} < 0.70$	1 413 738	0.097	1.043 ± 0.078
4	$0.70 \le z_{\mathrm{DNF}} < 0.85$	1 783 834	0.123	1.209 ± 0.081
5	$0.85 \le z_{\mathrm{DNF}} < 0.95$	1 391 521	0.096	1.451 ± 0.144
6	$0.95 \le z_{\mathrm{DNF}} < 1.05$	1 409 280	0.097	1.416 ± 0.125

$n(z)$ estimations and w_{ur} measurements apply these weights to counts of source galaxies as well. Magnification coefficients for the Metadetect bins are evaluated in [39]. The properties of the source galaxies in each tomographic bin generated in [27] are summarized in Table I.

2. MagLim++

The lens galaxy catalog we calibrate in this work is the Y6 MagLim++ catalog presented in [50]. The MagLim++ selection in DES Y6 refines the Y3 MagLim sample to improve purity and mitigate systematics. It consists of a magnitude-redshift cut, near-infrared (NIR) star-galaxy separation optimized for each redshift bin, and a SOM-based quality filter.

Galaxies are selected from the Gold catalog using i-band limiting magnitude thresholds,

$$i < 4 \times z_{\mathrm{DNF}} + 18, \qquad i > 17.5 \tag{26}$$

with z_{DNF} being the mean directional neighborhood fitting (DNF) [62] redshift estimates. This selection has been optimized to balance photometric redshift accuracy and number density, with the goal of to enhance the cosmological constraints on Ω_{m}, σ_8, and w [63]. Following [64], redshift-bin-optimized cuts in the $(r - z, z - W1)$ color space are used to isolate and remove stars from each bin, where $W1$ is a NIR magnitude from the unWISE catalog [65].

A SOM trained on $griz$ photometry is used to identify and remove galaxies in regions of color space with highly unreliable photometric redshifts, preferentially excluding quasars and other interlopers. The final sample is divided into six tomographic bins based on the DNF mean photometric redshift, with redshift bounds that yield similar sky density in each bin. The selection yields 9 186 205 galaxies. These refinements reduce stellar contamination, improve clustering signal fidelity, and enhance suitability for cosmological analyses.

The lens galaxies in each bin are summarized in Table II. We apply the LSS weights described in [50] to each galaxy during all WZ calculations and use magnification coefficient estimates from [39]. The characterization of the $n(z)$ using SOMPZ is described in detail in [28].

TABLE III. List of the spectroscopic samples from BOSS/eBOSS overlapping with the DES Y6 footprint and covering redshift up to 2.2, used as reference galaxies in this work.

Tracers	z range	N galaxies	Area (deg^2)
LOWZ + CMASS*	$0. \le z_{\mathrm{spec}} < 0.6$	88 340	860
CMASS** + LRG	$0.6 \le z_{\mathrm{spec}} < 1$	39 049	860; 700
ELG (eBOSS)	$0.5 \le z_{\mathrm{spec}} < 1.1$	86 055	620
QSO (eBOSS)	$0.8 \le z_{\mathrm{spec}} < 2.2$	20 837	700

B. Reference data

For all unknown samples (sources and lenses), we use as WZ references samples the spectroscopic galaxies from the BOSS and eBOSS surveys [33,34]. We also use the final eBOSS QSO sample covering $0.8 < z < 2.2$ [66] to extend WZ coverage to higher redshift. The DES Y3 analyses did not use the QSO samples.

The redshift range, number of galaxies, and DES overlap for each spectroscopic reference set are reported in Table III, and their redshift distributions are plotted in Fig. 3. We make use of the official random (unclustered) catalogs for all the different samples, paying attention that the ratio of random per tracer sample is constant, equal to 20. The weight for a BOSS-eBOSS galaxy i is calculated from the catalog weights as in [67]: $w^i_{\mathrm{tot}} = w^i_{\mathrm{noz}} w^i_{\mathrm{sys}} w^i_{\mathrm{CP}}$. There are no values available for BOSS-eBOSS magnification parameters α_{r}, so we assume Gaussian priors centered at $\alpha = 0$ with $\sigma = 2$.

1. BOSS-eBOSS galaxies

As in [10,15,17], we make use of the LOWZ, CMASS, eBOSS luminous red galaxies (LRG), and emission line galaxies (ELG) samples, covering a common sky area with DES. To avoid replication, we use a $z < 0.6$ truncated version of CMASS (that we refer to as CMASS*), and a $z > 0.6$ combination of CMASS (CMASS**) with eBOSS LRG. LOWZ, CMASS, and eBOSS LRG are composed of red galaxies located at $z < 1$. In addition, we use the eBOSS ELG sample covering $0.5 < z < 1.1$.

2. eBOSS QSO

In this work, in addition to these $z < 1.1$ samples, we use all the eBOSS QSOs, covering $0.8 < z < 2.2$. As McQuinn and White [18] demonstrate, the reconstructed $n(z)$ uncertainties scale at leading order with the number of reference objects, which is relatively low for the eBOSS QSOs. We thus use broader redshift bins for QSOs than low-z samples to raise signal-to-noise levels. Peculiar velocities of quasars are much larger than standard galaxies', but as we are dealing with angular correlations, the redshift-space-distortion effects are very limited [24]. We exclude scales $r_\mathrm{p} < 1.5$ Mpc.

C. CARDINAL simulated data

Construction of the CARDINAL simulation and the associated data are described in [45,68]. Here, we briefly summarize important features. CARDINAL is developed to produce realistic galaxy populations and lensing signals mimicking the DES Y6. As a successor to the Buzzard simulation [69], CARDINAL builds on a $10,000\ \mathrm{deg}^2$ light cone from $z = 0$ to $z = 2.35$ generated by combining three N-body simulations of varying resolutions. Galaxy properties, including positions, velocities, and magnitudes, are assigned to each dark matter particle based on their Lagrangian overdensities calculated in the initial condition of the simulation (inverse distance to the k nearest particles). The relation of galaxy properties to the Lagrangian overdensities is obtained from a subhalo abundance matching (SHAM) model constrained by the galaxy-galaxy correlations and group-galaxy correlations measured in SDSS [70]. An important feature of CARDINAL's SHAM model is the inclusion of orphan subhalos, enhancing the fidelity of galaxy clustering down to small scales. Lensing quantities such as shear, magnification, and deflections are computed using multiplane ray tracing [71], with an innovative hybrid correction scheme mitigating resolution effects [45]. The simulation also includes realistic photometric noise, modeled using DES Y6 survey property maps, ensuring that galaxy selection functions accurately mimic survey data.

The source galaxies in CARDINAL are selected based on *griz* photometry and PSF-convolved sizes, ensuring a number density consistent with the DES Y6 Metadetect sample. A key innovation in CARDINAL is the incorporation of spatial fluctuations driven by survey depth variations, implemented via a novel abundance matching algorithm [68]. The tomographic binning and redshift distribution of source galaxies are derived using the end-to-end DES SOMPZ framework.

To construct the MagLim++ lens galaxy sample in CARDINAL, we run a customized DNF pipeline on the entire catalog. As in DES Y6, MagLim++ samples are selected primarily based on i-band photometry. However, due to differences in photometry between the datasets, we adjust the magnitude cut to ensure that the MagLim++ sample in CARDINAL maintains a number density comparable to the DES Y6 MagLim++ sample within each tomographic bin.

We constructed a simulated BOSS-eBOSS sample using the simulated MagLim++ sample, selecting subsamples matching each data reference bin's redshift distribution and using true redshifts as the mock spectroscopic observations, since the impact of peculiar velocities on the spectroscopic samples is negligible for WZ [24]. The BOSS-eBOSS randoms are used to create a BOSS-eBOSS mask in CARDINAL, so that the sky distribution is also similar.

Initially, we built different BOSS-eBOSS mocks. The mock ELG catalogs consisted of blue galaxies, while the mock LOWZ-CMASS-LRG catalogs was composed of red galaxies, both selected with a similar selection in CARDINAL as with the data (cf. Appendix A). With these color-realistic mocks we measured that the galaxy biases from cross-correlations of sub-bins did not match the product of the galaxy biases inferred from autocorrelations,

$$w_{\mathrm{u}_i\mathrm{r}_i} \neq \sqrt{w_{\mathrm{u}_i\mathrm{u}_i} w_{\mathrm{r}_i\mathrm{r}_i}}. \tag{27}$$

A similar behavior was observed in [24] using the Flagship 2 simulation, on scales smaller than 1.5 Mpc, and interpreted as evidence of 1-halo effects impacting galaxy-bias measurements. In CARDINAL, we find the amplitude of this effect to be very large, with biases differing by up to a factor of 3–5 and effect persisted up to linear scales of 10 Mpc, whereas a 1-halo origin would suggest it should be confined to scales comparable to the typical 1-halo size (∼1 Mpc). Consistency between scales evaluated on data suggests that the behavior observed in Appendix A was due to the mismodeling of galaxy-halo properties in CARDINAL, rather than a physical process. Furthermore, in Appendix B 1, we measure the consistency between biases from auto- and cross-correlations for some red and blue samples constructed with Redmagic and MagLim++ data samples, and obtain the same results as in [24], namely this effect is limited to $r_\mathrm{p} < 1.5$ Mpc. Constructing the spectroscopic mocks using a subsample of the simulated MagLim++ catalog, we found this discrepancy between biases to be limited and in better agreement with previous works (e.g., [24]) and our data test (cf. Appendixes A and B 1). Thus, we decided to use the MagLim++-selected BOSS-eBOSS mocks.

IV. RESULTS

A. Systematics with CARDINAL

Systematics identified. The first step in our analysis is to use simulated samples to define the priors of the systematic parameters $s_{\mathrm{u}k}$. This procedure must be carried out for both source and lens samples. We identify several clustering redshift systematics that could impact our measurements:

(i) Any redshift evolution of the bias for the unknown sample, $b_\mathrm{u}(z)$, is not incorporated into the model.
(ii) At our scale range, $r_\mathrm{p} \in [1.5, 5]$ Mpc, modeling the galaxies as having linear bias with respect to the nonlinear matter power spectrum is not fully accurate [72,73]. Additional effects from 1-halo physics may be present, but they are expected to be minor at scales larger than 1.5 Mpc [24].
(iii) Simulations show that the correlation of spectroscopic galaxies from narrow redshift bins with photometric galaxies from broader bins can deviate from model prediction, because of the correlation at the border of the spectroscopic bin (cf. "Limber-1-bin approximation" in [24]). Our new clustering modeling [cf. Eq. (9)] is expected to correct for this effect; the clustering matrix A is not diagonal and takes into account correlation at the edges of the bins.
(iv) The use of the DP estimator instead of LS for source galaxies, in the cases where we lack the associated random catalogs, can cause larger biases in w_ur associated with mask shapes and edge effects. LS is known to be a better estimator than DP, with smaller bias and variance [74,75].

We note that a potential systematic we do not include in CARDINAL is the fiber collisions' effect on the spectroscopic samples.[9] Because of the fibers' diameters, two spectroscopic galaxies cannot be arbitrarily close, and the biases inferred from the autocorrelation might be underestimated with respect to the one from cross-correlation (which is not affected by this problem once weights are applied). We check this in Sec. IV B 2 by comparing the b_r obtained from different ranges of angular separation. Another potential systematic arises from assuming an incorrect cosmology when evaluating w_m [see Eq. (4)] through the Alcock-Paczynski effect. The quantity entering our modeling is $\sqrt{w_\mathrm{m}}$. Any constant offset with redshift is absorbed by the free amplitude b_u [see Eq. (24)], so only the redshift evolution of this ratio is relevant. We find that the ratio of this quantity computed assuming different cosmologies (DES Y3, KiDS Legacy, and Planck 2018) varies at the $\sim$1% level, which is negligible compared to the other systematics considered here.

Evaluating the effect of the systematics on WZ. We evaluate the systematic effects in CARDINAL by calculating the ratio of the measured w_ur to a model $\hat{w}_\mathrm{ur}$. Systematic effects can enter either the measurement w or the model $\hat{w}$. We execute the WZ analysis on CARDINAL data under two different cases. In the first "no-systematics" case we will "cheat" by using the truth values for certain quantities that we do not know for the real data, to see if this eliminates the expected systematic errors. In the second "all-systematics" case, we will impose the same level of ignorance on the CARDINAL catalog and parameters as we have for the real observations. Please note that we may underestimate cosmic variance in the no-systematics case since the true redshift distribution of the bins is taken directly from the full CARDINAL simulation, whereas real data are restricted to the 700 deg^2 of sky overlapping with BOSS-eBOSS mocks. The $n(z)$ measured in the presence of systematics are no longer expected to be normalized to unity.

The no-systematics test makes the following alterations to the mock catalogs:

(i) The model $\hat{w}_\mathrm{ur}$ departs from Eq. (17) by dropping the $(1+S)$ systematic correction term and the magnification terms. We replace $b_\mathrm{u} b_{\mathrm{r}_i}$ with $b_{\mathrm{u}_i} b_{\mathrm{r}_i}$, where b_{u_i} are estimated directly from a cross-correlation between r_i and the members of u that match the redshift range of r_i. Doing so should eliminate systematic errors associated with redshift evolution of bias and also limit the impact of scale-dependent bias from small-scale physics.
(ii) For each cross-correlation between the u bin and a reference bin r_i, we replace the u bin with an idealized bin. This is done by replacing each galaxy whose true redshift falls outside the redshift range of the reference bin with a randomly placed galaxies. This should correct for the "full-u-bin" systematic [24].
(iii) We use the LS estimator for w_ur, to have minimal variance and bias from the estimator.

Together, these alterations should guarantee that the measured w_ur are proportional to $n(z)$, within statistical uncertainties, if our code and methodology are correct.

For the all-systematics case, the analysis follows that of the real data:

(i) We use the DP estimator for sources; but we keep the LS estimator for lenses as we do have lens randoms.
(ii) We evaluate the cross-correlation w_{ur_i} using the full-u-bin's catalog instead of one with positions randomized outside the r_i bin redshift range.
(iii) We maintain the single unknown b_u value instead of using truth values for b_{u_i} in the model.

From now on, the different systematic functions will be referred as Sys.

Dominant systematic. We find the redshift evolution of galaxy bias to be the dominant systematic error causing a significant deviation from the model. As the other systematics have limited (if not null) impact, we do not separately analyze the different systematics as mentioned in Sec. II A 3. In particular, we found the full-u-bin systematics to have little impact for our analysis. Either our modeling of cross-correlations between bins—cf. Eq. (9)—has captured the effect, or our precision, using 700 deg^2 of BOSS-eBOSS data, is not good enough to detect these small effects, contrary to [24], for which they were considering cross-correlations between 1000 deg^2 of Euclid and DESI data.

1. Systematic function for MagLim++

In Fig. 4, we compare the true redshift distributions $n(z)$ of the six MagLim++ bins in the CARDINAL simulation with

[9] See https://www.sdss3.org/dr9/algorithms/boss_tiling.php.

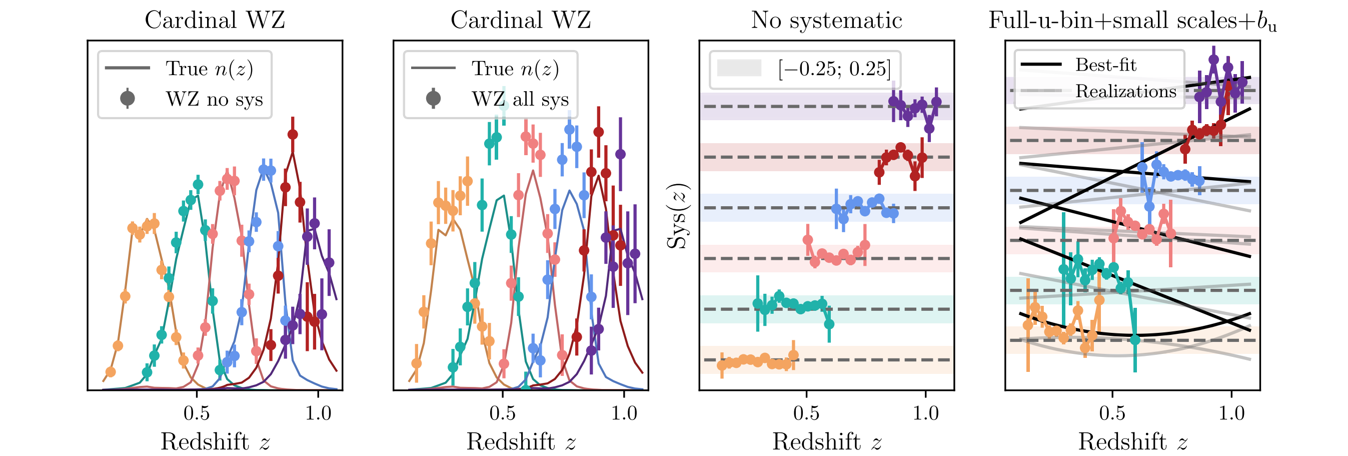

FIG. 4. Impact of systematics on WZ for the CARDINAL-simulated MagLim++ samples. Left: redshift distributions inferred from the no-systematics mock catalog, WZ estimate (points) compared to the true $n(z)$ (solid lines). Middle left: same as left but with the all-systematics mock catalog that uses only information available in the real data. Middle right: corresponding systematic function $w/\hat{w}$, for the no-systematic analysis, consistent with no deviation from a normalization constant. Right: systematic function $w(z)/\hat{w}(z)$ in the presence of systematics, where deviations from unity S_{ur_i} are fitted using a Legendre polynomial basis (black lines). The gray lines plot some realizations of S_{ur_i} from the derived prior on its s_{uk} coefficients.

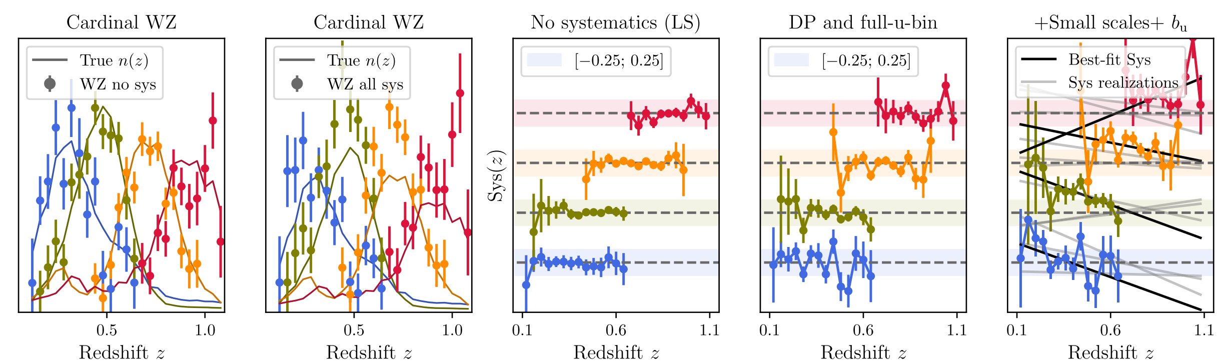

FIG. 5. Impact of systematics on WZ for the CARDINAL-simulated Metadetect samples. Left: redshift distributions inferred from the no-systematics mock catalog, WZ estimate (points) compared to the true $n(z)$ (solid lines). Middle left: same as left but with the all-systematics mock catalog that uses only information available in the real data. Middle: corresponding systematic function $w/\hat{w}$, for the no-systematic analysis, consistent with no deviation from a normalization constant. Middle right and right: systematic function $w(z)/\hat{w}(z)$ in the presence of systematics, where deviations from unity S_{ur_i} are fitted using a Legendre polynomial basis (black lines). The gray lines plot some realizations of S_{ur_i} from the derived prior on its s_{uk} coefficients.

the $n(z)$ inferred from WZ, in the no- and all-systematics cases, and the corresponding derived systematic correction function S_{ur_i} needed to force agreement between the model and mock data.

In the no-systematics case, the inferred distributions accurately recover the true distributions for all six bins. Small deviations at the peak of the Gaussian can be explained by binning effects, as illustrated in Fig. 3 of [24], and these are accounted for in the modeling of A_{rn}.

For the more realistic, all-systematics mock catalog, we observe significant deviations from the truth in the inferred $n(z)$. The corresponding S_{ur_i} corrections are shown in the right panel of Fig. 4. We model these systematic functions and find that an order-2 polynomial provides a good fit for bin 1, while an order-1 polynomial is sufficient for bins 2–6. We note that the largest impact of systematics in the first bin could be linked to a broader range of galaxy luminosities selected, leading to more complex redshift-dependent bias evolution. The priors on the nuisance parameters s_{uk} for the real data are chosen to follow a Gaussian distribution, centered at zero, with the standard deviation set to the best-fit parameter amplitude (i.e., the 1σ value). An alternative choice could have been to choose a Gaussian distribution centered at the best fit from CARDINAL, with same width, so that the no-systematic case is at 1σ. The implicit assumption for such case would be that we trust CARDINAL to reproduce the WZ systematics. We decided to rather assume CARDINAL was giving a

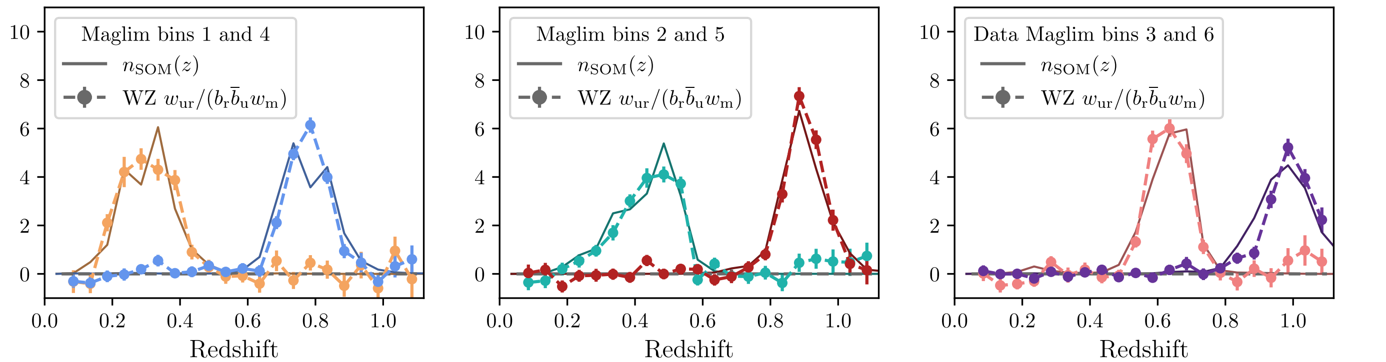

FIG. 6. The measured $n(z)$ from WZ $[= w_{\mathrm{ur}}/(b_{\mathrm{r}}b_{\mathrm{u}}w_{\mathrm{m}})]$ for each of the six DES Y6 data MagLim++ bins, without magnification and systematics modeling. BOSS and eBOSS samples, except QSO, are used as reference samples. The estimated $n(z)$ from the SOM are reported with solid lines.

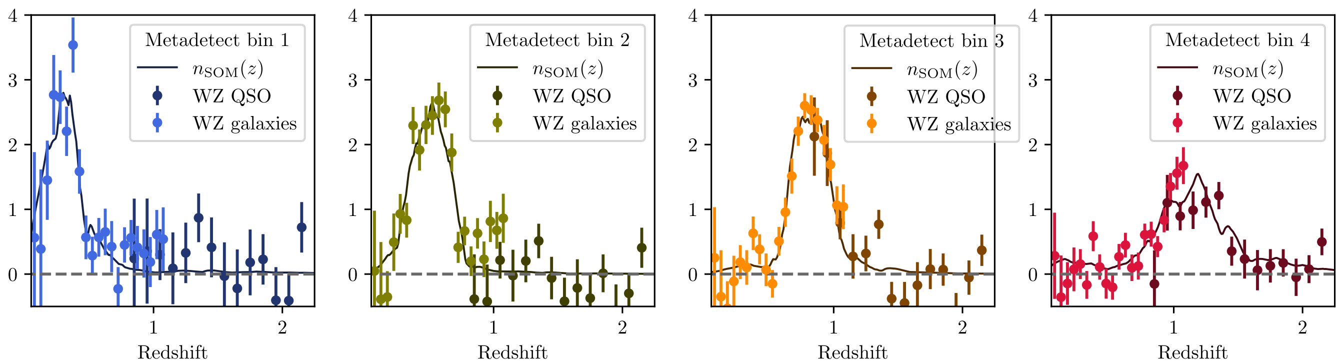

FIG. 7. The measured $n(z)$ from WZ $[= w_{\mathrm{ur}}(z)/(b_{\mathrm{r}}(z)\bar{b}_{\mathrm{u}}w_{\mathrm{m}}(z))]$ for each of the four DES Y6 data Metadetect bins, without magnification and systematics modeling. BOSS and eBOSS galaxies and QSO are used as reference samples separately, covering $0 < z < 2.2$. The estimated $n(z)$ from the SOM are reported with solid lines.

good estimate of the amplitude of the systematics, but was not necessarily reproducing them with fidelity.

Assuming consistency in the galaxy biases inferred from fiducial and large scales (as we will evaluate in Sec. IV B 2), the low order of the systematic functions is physically motivated. This is because the dominant systematic model error—redshift evolution of the galaxy bias—is expected to be small across the narrow redshift extent of the MagLim++ bins (cf. Sec. VI A for Y3 MagLim [63]).

2. Systematic function for Metadetect

In Fig. 5, we compare the true redshift distributions, $n(z)$, of the four CARDINAL-simulated Metadetect bins with the $n(z)$ inferred from WZ, in the no-systematics and all-systematics scenarios.

As with the MagLim++ simulations, the no-systematics mock catalog yields $n(z)$ consistent with the truth. When the realistic all-systematics catalog is used, however, we again observe significant deviations in the inferred $n(z)$. The corresponding S_{ur_i} corrections are shown in the right panel of Fig. 5. An order-1 polynomial provides an adequate fit for all four bins. As with MagLim++, the priors on the nuisance parameters for the real data are chosen to follow a Gaussian distribution centered at zero, with a standard deviation set to the amplitude of the best-fit CARDINAL parameters. A few realizations of the systematic functions drawn from these priors are also shown in the right panel. Even though the source bins are wider than the lens bins, we still find that linear systematic functions are effective at describing the dominant systematic error—redshift evolution of galaxy bias—across the bins.

B. Data calibration

1. Measurements

In Figs. 6 and 7, we present the WZ measurements $w_{\mathrm{ur}}/(b_{\mathrm{r}}b_{\mathrm{u}}w_{\mathrm{m}})$ for MagLim++ and Metadetect bins, overlaid on the SOM-derived $n(z)$. Here, b_{r} represents the galaxy bias of BOSS-eBOSS, which evolves with redshift, while b_{u} is the best-fit amplitude of the measurement relative to the SOM $n(z)$. We observe a visually reasonable agreement between WZ and the SOM estimates. We report in Appendix C the measurements for Metadetect and MagLim++ using DESI galaxies as reference. We obtain

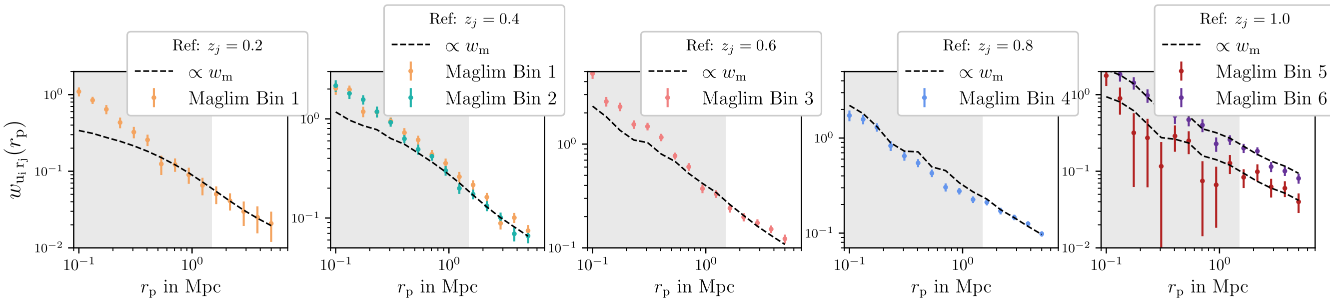

FIG. 8. Angular correlation vector for the six MagLim++ bins (colors) and five BOSS-eBOSS reference bins (panels), for angular scales corresponding to $r_p \in [0.1, 5]$ Mpc, and reference binning $\Delta z = 0.05$. We only plot nonzero correlations (i.e., combinations of u-r bins which overlap in redshift). We also plot a model $\hat{w}_{ur} = a \times w_m(r_p)$ for the best-fit constant a. The scales discarded for our WZ analysis ($r_p < 1.5$ Mpc) are colored in gray. We observe a good fit for the scale range [1.5, 5] Mpc, used in this work, despite the simplicity of the modeling.

an excellent agreement with BOSS-eBOSS measurements. We retain BOSS-eBOSS as our fiducial WZ measurements rather than slow the Y6KP analysis with a switch to DESI.

Figure 7 includes $z > 0.8$ clustering-redshift measurements using eBOSS-QSOs. Due to the sparse density of this tracer, we adopted a binning of $\Delta z = 0.1$ to increase the number of spectroscopic redshifts per bin, as the uncertainty on $n(z)$ scales with the number of available spec-z [18]. We detect no significant signal for bins 1 and 2, partially recover the right tail of the distribution for bin 3, and measure most of the distribution for bin 4. Although not highly precise, these measurements serve as a useful validation of the SOM's performance at high redshift.

As future surveys such as DESI and 4MOST will provide significantly more QSOs up to $z \sim 3$, this measurement serves as a promising proof of concept for high-z calibration in upcoming LSST and Euclid [76,77].

2. Scales and galaxy biases

For clustering redshifts, we rely on small scales that are not used for cosmological analyses due to the lack of precise modeling. Therefore, it is crucial to test whether these scales can still be reliably used for redshift calibration. A detailed investigation of the impact of small-scale effects on WZ measurements can be found in Sec. 4.3 of [24]. The main conclusion of that work is that deviations of $w(z)$ from a model adopting linear, redshift-independent bias for the unknown populations are small enough to be corrected by our systematic-error functions for our chosen scale range of $1.5 \le r_p \le 5$ Mpc. The lower bound is a compromise between measurement precision and modeling accuracy, while the upper bound is fixed by the need to maintain statistical independence from the cosmological $w(\theta)$ measurements. As a check, we investigate here whether varying the scale range significantly affects the inferred $n(z)$. We examine three different scale ranges: small scales (SS), [0.1, 1.5] Mpc; fiducial range (Fid), [1.5, 5] Mpc; and large scales (LS), [5, 15] Mpc.

Nonlinear modeling. As a first sanity check, we examine $w_{ur}(\theta)$ to assess whether our model assumption of linear galaxy bias [cf. Eq. (3)] remains valid across the chosen $w(\theta)$ scales. Figure 8 shows the correlation measurements for MagLim++ bins cross-correlated with different spectroscopic bins, plotted as a function of scale from 0.1 to 5 Mpc.[10] When the MagLim++ bin and the reference bin overlap in redshift so that the $w_{ur}(\theta)$ is appreciable, we observe that the linear-bias fit remains visually good down to $r_p \approx 1$ Mpc, across redshifts.

Unknown galaxy bias. Two internal consistency checks on the validity of the linear-bias model [cf. Eq. (3)] and the modeling of the bias redshift evolution [cf. Eq. (17)] are possible. We examine the value of $\bar{b}_u$ for every bin that best fit the data with the simplified model

$$\hat{w}_{ur}(z_i) = \bar{b}_u b_r(z_i) n_u(z_i) w_m(z_i), \tag{28}$$

where we use the $n(z)$ derived from the SOMPZ method[11] and measure w_{ur} on the data for three scale ranges (SS, Fid, and LS). We know that the linear-bias model is valid for LS.

The robustness of the linear-bias assumption in the full $\hat{w}_{ur}$ model of Eq. (17) is supported by the agreement of the bias values between the Fid and LS scale-range choices, as reported in Fig. 9. For both MagLim++ and Metadetect, the differences between Fid and LS bias values are easily modeled by our systematic functions S_{ur_i}. The galaxy-bias measurements using small scales show strong deviation from the fiducial case. This is not unexpected, as we observe in Fig. 8 that the linear-bias model is insufficient at small scales. The large-scale galaxy-bias values for

[10] We do not show larger scales, as they are used for cosmology, and since we are not using a blinded catalog, we avoid unintentionally unblinding the Y6 data in this figure.

[11] For the importance sampling, we will get b_u for every realization, cf. Eq. (24) from a similar fitting, but considering systematics and magnification. For this test, we are assuming the SOM $n(z)$ if a good model, and focus on the galaxy biases.

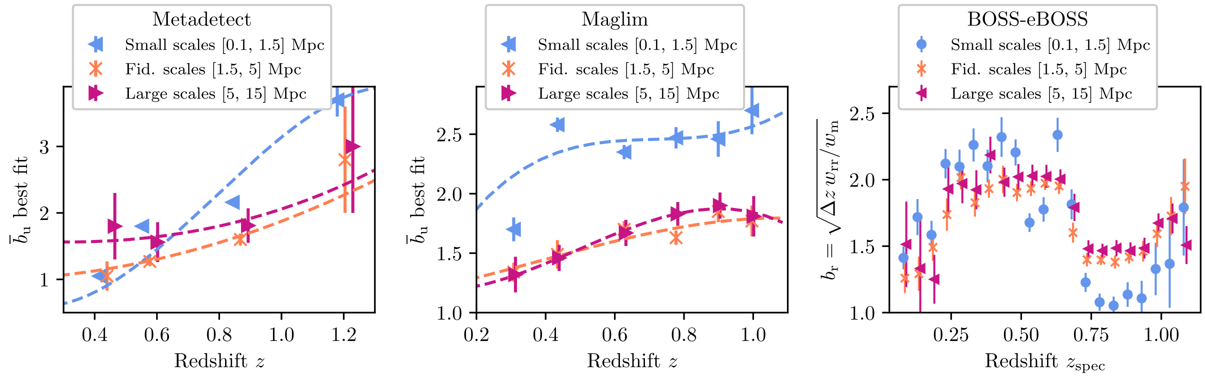

FIG. 9. Galaxy biases of the three samples used for DES Y6 WZ are plotted vs redshift. The values for Metadetect (left) and MagLim++ (middle) are derived from a fit of cross-correlations of each tomographic bin with BOSS-eBOSS galaxies [fixing $n_u(z)$ to $n_{SOM}(z)$, cf. Eq. (28)], and values for BOSS-eBOSS (right) from their autocorrelation. Each panel shows the average bias across three scale ranges: [0.1, 1.5] Mpc (SS, orange), [1.5, 5] Mpc (Fid, red), and [5, 15] Mpc (LS, purple). In each case, the Fid and LS biases are consistent and well fit by a low-order polynomial. The SS cases differ, due to some combination of nonlinear bias and, for BOSS-eBOSS, fiber collisions.

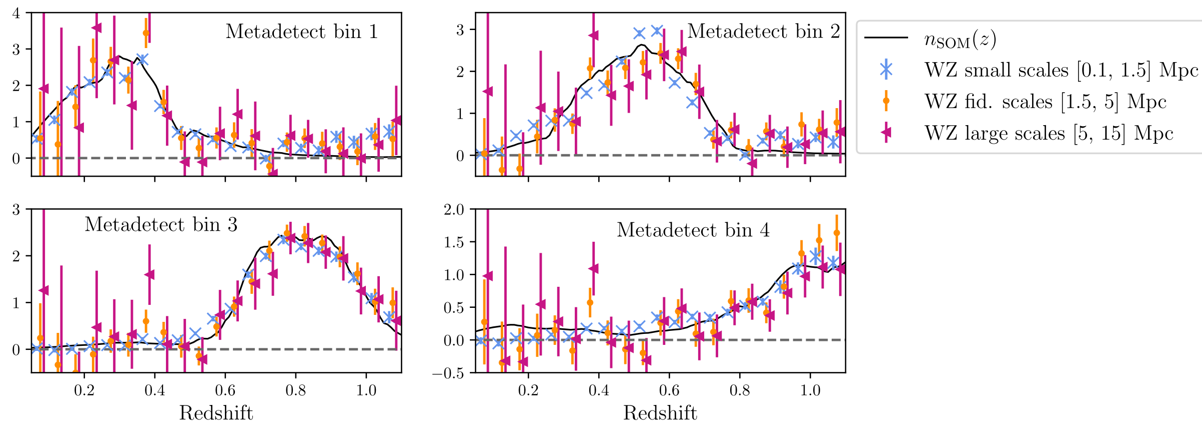

FIG. 10. Redshift distributions of Metadetect four bins, evaluated as $n(z) = w_{ur}(z)/(\bar{b}_u b_r(z) w_m(z))$ (so neglecting magnification and systematics), for three scale ranges. We can observe a very good agreement between the measurements using fiducial range [1.5, 5] Mpc (orange) and the large-scale range (red).

MagLim++ are consistent with those reported in the Y3 results (cf. Appendix B of [63]).

We can also use the $\bar{b}_u$ to crudely confirm that our chosen priors on the systematic-function coefficients s_{uk} introduce sufficient freedom to track the variation of the unknown samples' bias functions with redshift, if we assume that the variation of $\bar{b}_u$ between different lens or source tomographic bins is a good proxy for the evolution of $b_u(z)$ within each tomographic bin. This assumption is not expected to be very accurate, especially for Metadetect, because different color selection criteria are used for distinct bins, so their constituent galaxy populations differ. For MagLim++, as bins are defined with photo-z cuts, this procedure to estimate bias evolution corresponds to the method M3 in [24] and was found to be accurate (cf. their Fig. 14). Proceeding, we plot each $\bar{b}_u$ of each bin at the mean of its SOMPZ redshift distribution in Fig. 9. We observe that the redshift evolution of the galaxy bias for both the Fid and LS scale selections are well described by low-order polynomials and can be well fit using the priors and degrees for the systematic s_{uk} functions that we derived from the CARDINAL simulations in Sec. IV A.

Reference galaxy bias. Next we examine the consistency of the reference galaxy biases extracted from the autocorrelations. The right-hand panel of Fig. 9 shows the derived biases for BOSS-eBOSS vs redshift of the bin for the three choices of scale range. The Fid and LS cases agree very well, suggesting that neither scale-dependent bias nor fiber collisions are having substantial impact at the fiducial range. The SS biases differ substantially, suggesting the presence of one or both effects in the small-scale clustering data. The substantial changes in bias near $z = 0.2$ and $z = 0.7$ are expected from the changes in BOSS-eBOSS selection criteria.

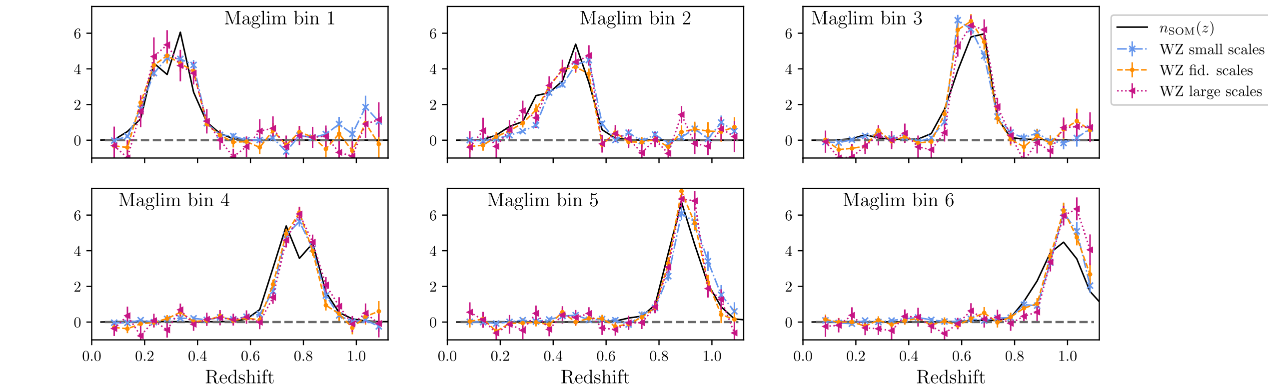

FIG. 11. Same as Fig. 10, for the six MagLim++ bins. We also observe an excellent agreement between fiducial and large-scale ranges.

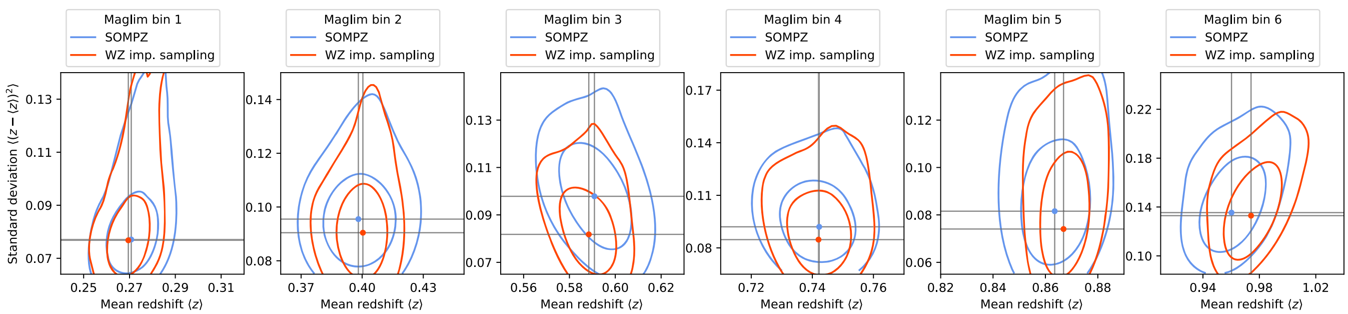

FIG. 12. Distributions of the mean redshift and standard deviation of $n(z)$ samples drawn from $p(n|\mathrm{PZ})$ using SOMPZ (blue) and samples drawn from $p(n|\mathrm{WZ},\mathrm{PZ})$ using WZ importance sampling (red), for each of the six MagLim++ tomographic bins. The contours represent 68% and 95% of the data points. The lines report the position of the peaks. The WZ selected $n(z)$ samples tend to have slightly lower standard deviations and slightly less variation in the mean. Only bin 6 shows a substantial shift in the derived mean redshift.

WZ and scales. Figures 10 and 11 compare the $n(z)$ values derived using the SS, Fid, and LS scale ranges for each Metadetect and MagLim++ bin, respectively, under the simplified model $n(z) = w_{\mathrm{ur}}(z)/(\bar{b}_{\mathrm{u}} b_{\mathrm{r}}(z) w_{\mathrm{m}}(z))$. The LS and Fid cases yield to two WZ results consistent within their statistical uncertainties. The SS WZ result often differs from the two others WZ results by substantially more than its (very small) statistical uncertainties. To quantify any scale-dependent deviations, we compute the ratio of the inferred redshift distributions between different scale ranges: $\eta_{\mathrm{scales}}(z) = n(z|\mathrm{scales}_1)/n(z|\mathrm{scales}_2)$, The results are shown in Appendix D. For both MagLim++ and Metadetect, and for Fid vs LS, we find that any differences are well within the freedom that we have allotted to the systematic-error function. We find no significant evidence that fiber collisions affect our results. Fiber collisions should impact autocorrelations more strongly than cross-correlations and primarily on small (fiducial) scales, however we obtain consistent galaxy biases from autocorrelations across both fiducial and large-scale ranges (cf. Fig. 9), as well as consistent $n(z)$ between these two scale choices (cf. Figs. 10 and 11). In addition, the $n(z)$ inferred from BOSS and eBOSS agrees with that obtained from DESI on the same scales, despite their different fiber-collision properties (cf. Appendix C). This is consistent with [78], where they showed that fiber collisions have limited impact even on 1–5 Mpc scales. Because of this, and taking into account that any residual effect can be absorbed by our systematic function, provided it does not vary too rapidly with redshift, we are not explicitly modeling fiber collision in this paper.

C. Importance sampling

We now turn to the results of applying the full WZ importance sampling process (cf. Sec. II D) to the samples of $n(z)$ produced by the SOMPZ + 3sDir photometric analyses.

For MagLim++, importance sampling of the SOMPZ $n(z)$ samples using the WZ likelihood is performed independently for the six lens bins. For each $n(z)$ sample, we compute the mean z and standard deviation of z. Distributions of these quantities computed from 100×10^6 input PZ samples, and from the few thousand selected via WZ, are reported in Fig. 12. The WZ information has led to negligible shifts in the mean redshift in bins 1–4, small shifts for bin 5, and a shift $\Delta\langle z\rangle \approx 0.015$ in bin 6. As seen in Fig. 6, this shift in bin 6 is primarily driven by a comparatively weak WZ signal at $z \sim 0.85$ relative to the

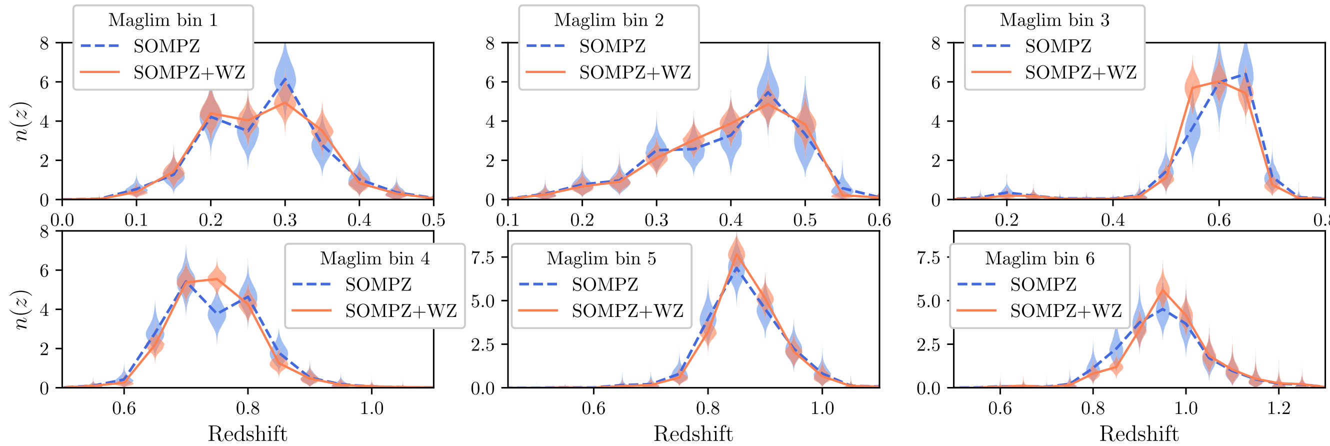

FIG. 13. Left: violin plots showing the distribution of $n(z)$ functions in each of the six MagLim++ bins. Blue violins and lines are the distributions and means of $n(z)$ taken directly from the 3sDir sampling. Red lines and violins represent similar quantities from the WZ selected subsample.

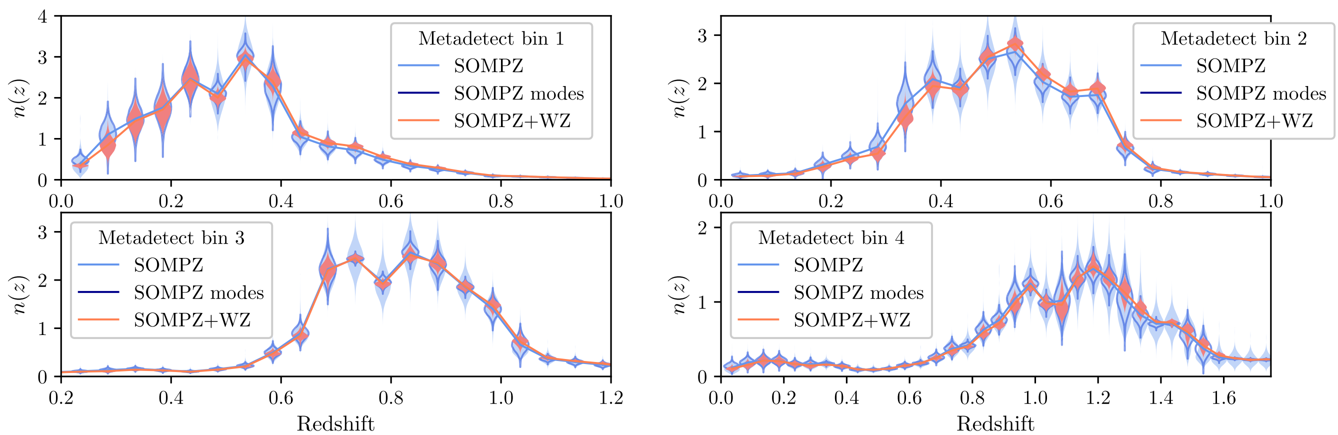

FIG. 14. Violin plots showing the distribution of $n(z)$ functions in each of the four Metadetect redshift bins. Blue violins and lines are the distributions and means of $n(z)$ taken directly from the 3sDir sampling. Dark blue contour violins have used mode projection to remove fluctuations with no significant cosmological impact (the mean is unchanged by this process). Orange are the distributions after importance sampling with the WZ likelihood.

SOM mean distribution. Bringing the WZ + PZ point at this z into agreement with the mean of the PZ values would require a multiplicative error of factor ≈ 3, restricted only to this point, which is not within the realm of WZ systematic errors expected nor encountered in CARDINAL. As $z \sim 0.85$ corresponds to the transition in the reference sample between an LRG dominated sample and an ELG dominated sample, we rerun WZ for both LRG and ELG separately and report the results in Appendix B 2. Both reference samples, composed of the same galaxy tracer, are in good agreement. We thus consider this shift of the bin 6 leading edge to be a definitive implication of the WZ measurement. Regarding the standard deviation of $n(z)$, WZ information alters the results of PZ sampling noticeably only by requiring a narrower $n(z)$ for bin 3.

Figure 13 presents violin plots of the distributions of MagLim++ $n(z)$ before and after WZ importance sampling. We observe that incorporating WZ information yields smoother $n(z)$ distributions, removing the "divots" in $n(z)$ in bins 1, 2, and 4. Additionally, the sizes of the violins are reduced, as WZ sampling eliminates $n(z)$ samples from PZ that have nonphysical fluctuations, i.e., the typical $n(z)$ samples are less noisy after WZ importance sampling.

For Metadetect source redshifts, as explained in Sec. II D, we first remove cosmologically irrelevant fluctuations from the input SOMPZ $n(z)$ samples to ensure that importance sampling yields a sufficiently large output sample. Figure 14 compares the uncertainties in the PZ + WZ $n(z)$ elements with those in the PZ-only case, both before and after mode compression of the PZ samples.

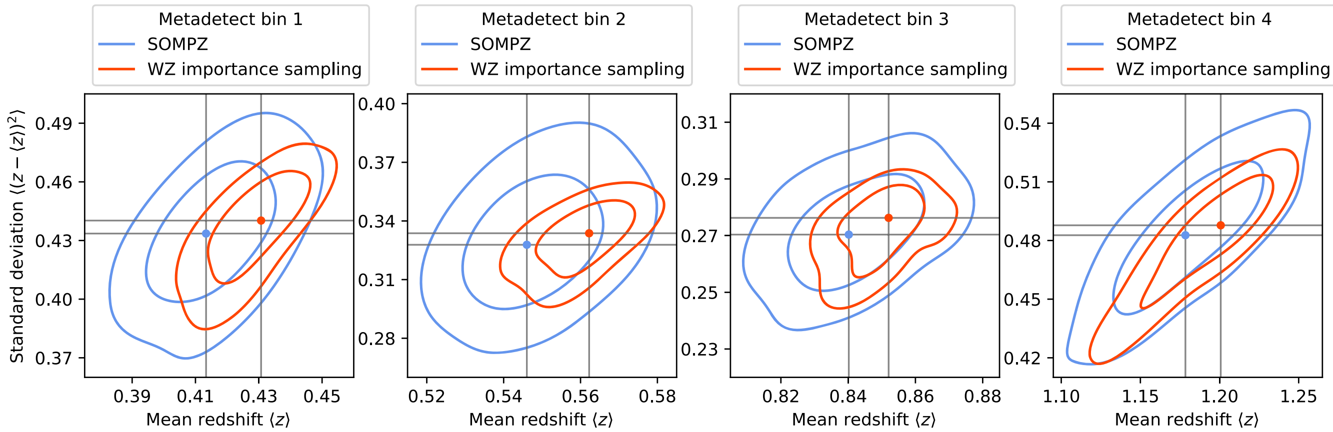

FIG. 15. Same as Fig. 12 for Metadetect four bins. Samples drawn from p(n|PZ) are reported in blue, and samples drawn from the importance sampling on the compressed PZ are reported in red. Contrary to MagLim++, here WZ has an impact on the mean redshift of the selected samples, with preference for higher mean redshifts. The variations in standard deviation is also reduced with a preference for larger bins.

As expected, mode compression significantly reduces fluctuations in $n(z)$ at each redshift, i.e., the violins are shorter. The addition of WZ selection further suppresses fluctuations, in line with expectations.

For the four source redshift bins, Fig. 15 shows the distributions of the mean redshift $\langle z \rangle$ and standard deviation std(z) across two cases: the original 3sDir samples and compressed PZ + WZ samples selected with importance sampling. The most noticeable feature is an upward shift of approximately 1σ in $\langle z \rangle$ bins 1 and 2, and a moderate upward shift for bins 3 and 4, due to WZ data, along with a increase of the standard deviation of $n(z)$ (larger bin widths). We performed importance sampling with larger priors on the systematics function, to check whether the priors were not too small to describe the galaxy-bias evolution $b_{\mathrm{u}}(z)$, but we got similar shifts for all the bins.

In Fig. 16, we further investigate the cause of the shifts in mean z. We start with the mean $n(z)$ from the SOM and determine the best-fit model by varying the b_{u}, magnification and systematic parameters of $\hat{w}_{\mathrm{ur}}$ with respect to the BOSS WZ measurements. Using these best-fit parameters, we transform $w_{\mathrm{ur}}(z)$ into a redshift distribution,

$$n_{\mathrm{WZ}}(z) = (w_{\mathrm{ur}}(z) - w^{\mu}_{\mathrm{bf}})/(b_{\mathrm{r}} b_{u,\mathrm{bf}}), \tag{29}$$

where the magnification contribution w^{μ} to the covariance and the bias b_u are given their values in the best-fit model to the data. The resulting $n(z)$ distributions are shown in Fig. 16 and compared with the mean SOMPZ $n(z)$. For bin 3, the WZ-derived model is significantly narrower than the SOMPZ $n(z)$ but remains relatively centered. In contrast, for bins 1 and 2, the WZ-derived model fluctuates around the SOMPZ $n(z)$, possibly leading to the observed shift in mean z. Achieving full consistency between the SOM $n(z)$ and the best-fit model would require a higher-order systematic function, allowing for these to be oscillatory in the model, which is not physically motivated. Focusing on Fig. 16, it seems WZ is predicting an excess for the first two bins at $z \sim 1.05$, which could hint for a potential systematic, such as wrong magnification priors, leading to an underestimation of this effect. One can then naturally think these $z \sim 1$ WZ points are responsible of the mean-z shifts observed in Fig. 15. If we now look at Fig. 14, we see no excess on the WZ selected $n(z)$ at $z \sim 1$ with respect to PZ ones. For bins 1 and 2, the reason is straightforward: the PZ samples are only marginally deviating from 0 at $z = 1$, and thus the corresponding WZ data points have no effect for the importance sampling. For bins 3 and 4, there is no significant mismatch between the best-fit WZ $n(z)$ and the SOM one [which does not correspond to the true $n(z)$], showing that if there was a localized systematic effect, it is corrected by the Sys function. A closer investigation reveals that this shift primarily arises because the WZ data favor 3sDir samples from regions in the Latin hypercube where COSMOS and PAUS redshifts have been perturbed upward, though still within their estimated uncertainties.

D. Impact on cosmology

In this section, we assess the impact of including WZ information on cosmological constraints. Specifically, we aim to answer two key questions: (1) Does incorporating WZ information shift the peak of the posterior distributions of cosmological parameters? (2) Does it reduce the size of the posterior contours? To investigate these effects, we analyze two sets of Markov chain Monte Carlo runs: one considering cosmic shear (CS, 1×2pt) alone and one with galaxy clustering, galaxy-galaxy lensing, and cosmic shear (3×2pt). The marginalization over photometric uncertainties follows the mode-based approach described in Sec. II D, replacing the shift-and-stretch model used in Y3. The data vector is generated assuming a flat ΛCDM

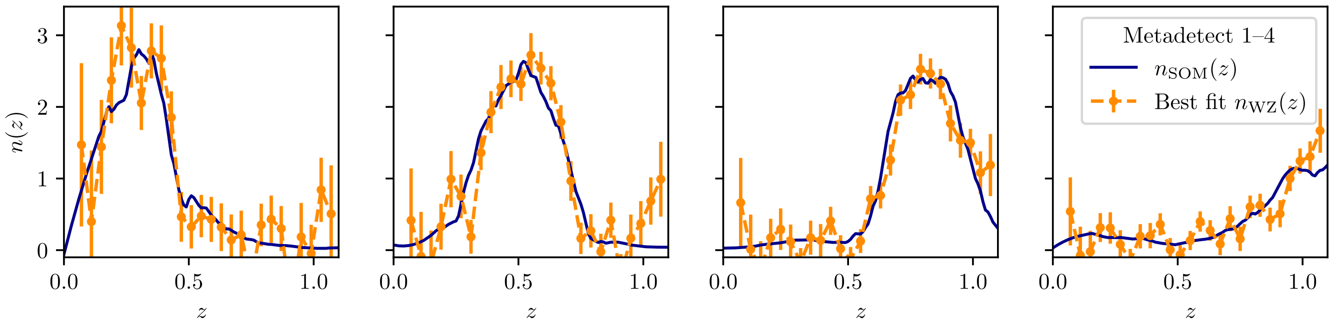

FIG. 16. The $n(z)$ from the SOM and the best-fit distribution from the WZ data for Metadetect four bins (including magnification, bias, and systematic parameters). One can see that, for the first two bins, the best model oscillates around the SOM distribution which does not capture some of the high-z features in the WZ best fit (e.g., for the second bin, the excess at $z \sim 0.55$).

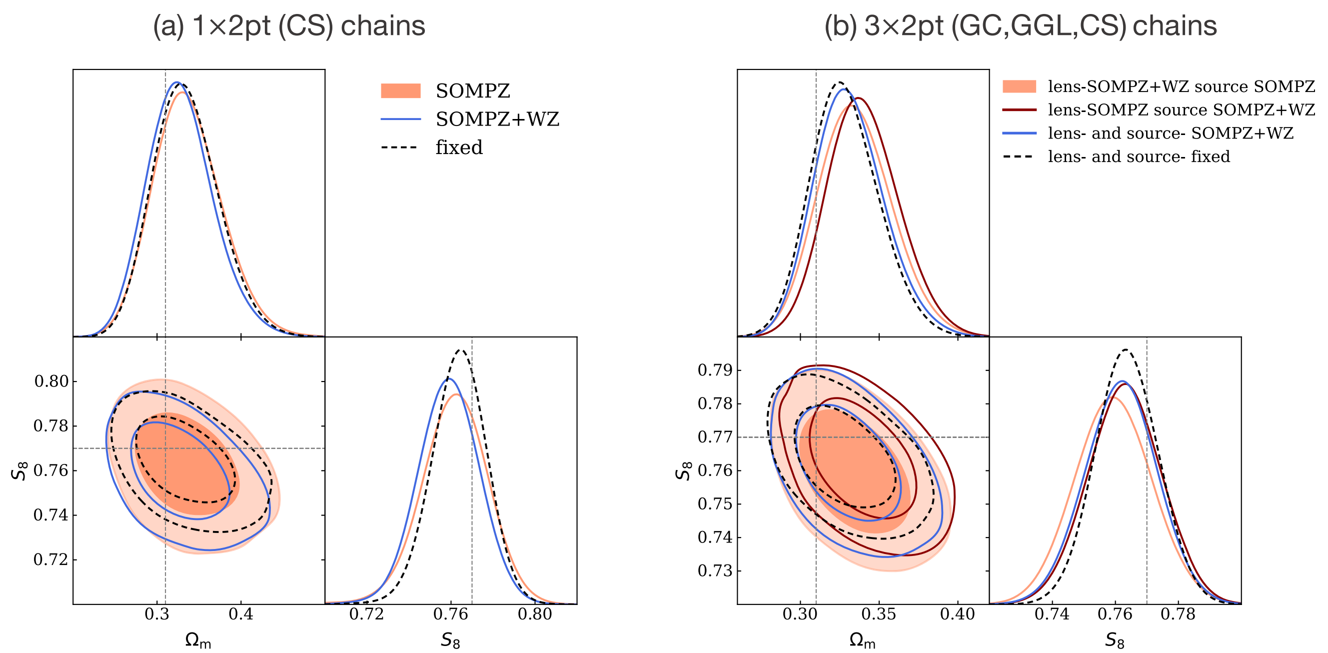

FIG. 17. (a) Cosmic shear (1×2pt) chains for three setups: SOMPZ uncertainty in orange, SOMPZ + WZ uncertainty in blue, and fixed (i.e., no uncertainty) in black. We see a significant gain on S_8 adding WZ uncertainty, but still smaller constraining power in comparison to fixed. All the three chains give consistent results. (b) 3×2pt chains for the four uncertainty setups: lens SOMPZ + WZ and source SOMPZ in orange, lens SOMPZ and source SOMPZ + WZ in red, both lens and source with SOMPZ + WZ in blue, and both lens and source fixed (i.e., no uncertainty) in black. All the chains give consistent results, with a clear gain adding WZ information, mainly for the source.

cosmology ($\Omega_m = 0.31$, $A_s 10^9 = 1.831$, $n_s = 0.965$, $\Omega_b = 0.051$, $h = 0.69$) and, for both lenses and sources, assumes a true $n(z)$ that is the mean of our derived sampling of $p(n|\mathrm{WZ}, \mathrm{PZ})$.

1. Cosmic shear

We test three setups for the source uncertainties assumed for the cosmological inference:

(i) SOMPZ: the $n(z)$ modes and priors are derived from compression of the full SOMPZ samples from $p(n|\mathrm{PZ})$;
(ii) SOMPZ + WZ: the $n(z)$ modes and priors are derived from the importance-sampled $p(n|\mathrm{WZ}, \mathrm{PZ})$;
(iii) fixed: no photo-z uncertainties are marginalized over.

The posterior distributions of CS chains are shown in Fig. 17(a). Incorporating WZ calibration of sources using the BOSS-selected sample improves the constraints in S_8 by 10% in the cosmic shear analysis. The fixed posteriors improves SOMPZ + WZ constraints in S_8 by 10%, meaning we are still losing some constraining power because of the redshift uncertainties. We observe consistency between the three results. SOMPZ and WZ are expected to provide consistent best-fit cosmological parameters, with the inclusion of WZ leading to improved constraints.

2. 3×2pt

For lenses and sources, we have modes and priors derived from $p(n|\mathrm{PZ})$ referred to as SOMPZ and from the WZ-importance-sampled $p(n|\mathrm{WZ},\mathrm{PZ})$ referred to as SOMPZ+ WZ. We then test four setups for the uncertainties:

(i) source SOMPZ and lens SOMPZ + WZ,
(ii) source SOMPZ + WZ and lens SOMPZ,
(iii) source SOMPZ + WZ and lens SOMPZ + WZ,
(iv) fixed: no photo-z uncertainty are marginalized over for both lens and source.

The posterior distributions of 3×2pt chains are shown in Fig. 17(b). Adding the WZ information, we observe a gain of around 10% in S_8. Comparing the combinations of SOMPZ and SOMPZ + WZ uncertainty, we see that this gain is mainly coming from the uncertainties of sources (orange vs red), and adding WZ for lenses has a negligible impact in S_8 (red vs blue), but results in a small gain in Ω_m. The fixed posteriors improves SOMPZ + WZ constraints in S_8 by 15%, meaning we are still losing significant constraining power because of the redshift uncertainties. We observe consistency between the results. SOMPZ and WZ are expected to provide consistent best-fit cosmological parameters, with the inclusion of WZ leading to improved constraints.

V. CONCLUSION

This work is part of a series establishing the redshift calibration for the DES Y6 3×2pt cosmology analysis. Photometric redshifts in DES Y6 are estimated using SOMs, calibrated with spectroscopic and many-band photometric data, as described in [27,28]. In this paper, we complement these estimates with clustering-based redshift (WZ) constraints by cross-correlating DES galaxies with BOSS, eBOSS, and eBOSS quasar samples. These angular cross-correlations define a WZ likelihood, which is then used to perform importance sampling on a large ensemble of SOM-derived $n(z)$ realizations, retaining those consistent with the WZ measurements. The resulting posterior samples of $n(z)$ for each lens and source bin are then compressed using a principal component analysis-like decomposition introduced in [29], enabling efficient exploration within cosmological parameter inference.

Our main contributions include:

(i) Introducing the WZ methodology for DES Y6, including a redshift decomposition [cf. Eq. (7)], magnification [cf. Eq. (13)], and a systematics model [cf. Eq. (18)]. All combined, we can express our WZ data vectors as linear combinations of analytical quantities—cf. Eq. (17).
(ii) Presenting an analytically marginalizable WZ likelihood that incorporates systematics and magnification [cf. Eq. (21)], allowing direct sampling of $n(z)$ realizations consistent with both SOMPZ and WZ constraints—cf. Sec. II D.
(iii) Investigating the impact of modeling systematics using CARDINAL mocks and showing that a low-order polynomial bias evolution model (linear or quadratic) is sufficient for DES Y6 and significantly simpler than the fifth-order model used in DES Y3—cf. Sec. IV A.
(iv) Performing cross-correlation measurements using BOSS and eBOSS galaxy and quasar samples—cf. Sec. IV B 1.
(v) Comparing our redshift measurements with DESI, showing consistency and confirming the reliability of the method—cf. Appendix C.
(vi) Validating the scale range used in the analysis, demonstrating robustness to nonlinear and small-scale effects—cf. Sec. IV B 2 and Appendix D.
(vii) Applying importance sampling, significantly reducing redshift uncertainties by selecting realizations consistent with clustering data—cf. Sec. IV C.
(viii) Demonstrating that incorporating WZ leads to improved constraints on cosmological parameters in test chains—cf. Sec. IV D.

This work highlights the importance of clustering-based redshift constraints as a complement to photometric methods. While SOM-based methods remain a powerful baseline, combining them with WZ constraints improves robustness and reduces uncertainties. This hybrid approach will be crucial for future stage-IV surveys such as Euclid, LSST, and Roman, which will benefit from deeper imaging and much greater spectroscopic overlap. For instance, Euclid will obtain a spectroscopic redshift sample up to $z\sim 1.8$ with Hα emitters across its entire footprint. Even higher redshifts, up to $z\sim 3$, will be accessible through quasars with DESI. The methodology developed here is readily extensible to these surveys, paving the way for precise and reliable redshift calibration in next-generation cosmological analyses.

ACKNOWLEDGMENTS

We thank Cristobal Padilla for his support and advices, Jonas Chaves Montero for his comments on the small scales clustering and mock realism, and Andreu Font-Ribera for his comments relative to fiber collision. W. d'A. acknowledges support from the MICINN projects PID2019-111317GB-C32 and PID2022-141079NB-C32 as well as predoctoral program AGAUR-FI ajuts (2024 FI-1 00692) Joan Oró. IFAE is partially funded by the CERCA program of the Generalitat de Catalunya. G. M. B. acknowledges support from DOE Grant No. DE-SC0007901 and NSF Grant No. AST-2009210 during this work. M. M. acknowledges support from the MINCINN Grants No. CNS2023-144328 (CARTEU) and No. PID2022-141079NB-C32. The project that gave rise to these results received the support of a fellowship from "la Caixa" Foundation (ID 100010434). The fellowship code is LCF/BQ/PI23/11970028. Funding for the DES Projects has been provided by the U.S. Department of Energy, the U.S. National Science Foundation, the Ministry of Science and Education of Spain, the Science and Technology Facilities Council of the United Kingdom, the Higher Education Funding Council for England, the National Center for Supercomputing Applications at the University of Illinois at Urbana-Champaign, the Kavli Institute of Cosmological Physics at the University of Chicago, the Center for Cosmology and Astro-Particle Physics at The Ohio State University, the Mitchell Institute for Fundamental Physics and Astronomy at Texas A&M University, Financiadora de Estudos e Projetos, Fundação Carlos Chagas Filho de Amparo à Pesquisa do Estado do Rio de Janeiro, Conselho Nacional de Desenvolvimento Científico e Tecnológico and the Ministério da Ciência, Tecnologia e Inovação, the Deutsche Forschungsgemeinschaft, and the collaborating institutions in the Dark Energy Survey. The collaborating institutions are Argonne National Laboratory, the University of California at Santa Cruz, the University of Cambridge, Centro de Investigaciones Energéticas, Medioambientales y Tecnológicas-Madrid, the University of Chicago, University College London, the DES-Brazil Consortium, the University of Edinburgh, the Eidgenössische Technische Hochschule (ETH) Zürich, Fermi National Accelerator Laboratory, the University of Illinois at Urbana-Champaign, the Institut de Ciències de l'Espai (IEEC/CSIC), the Institut de Física d'Altes Energies, Lawrence Berkeley National Laboratory, the Ludwig-Maximilians Universität München and the associated Excellence Cluster Universe, the University of Michigan, NSF NOIRLab, the University of Nottingham, The Ohio State University, the University of Pennsylvania, the University of Portsmouth, SLAC National Accelerator Laboratory, Stanford University, the University of Sussex, Texas A&M University, and the OzDES Membership Consortium. Based in part on observations at NSF Cerro Tololo Inter-American Observatory at NSF NOIRLab (NOIRLab Prop. ID 2012B-0001; PI: J. Frieman), which is managed by the Association of Universities for Research in Astronomy (AURA) under a cooperative agreement with the National Science Foundation. The DES data management system is supported by the National Science Foundation under Grants No. AST-1138766 and No. AST-1536171. The DES participants from Spanish institutions are partially supported by MICINN under Grants No. PID2021-123012, No. PID2021-128989, No. PID2022-141079, No. SEV-2016-0588, No. CEX2020-001058-M, and No. CEX2020-001007-S, some of which include ERDF funds from the European Union. IFAE is partially funded by the CERCA program of the Generalitat de Catalunya. We acknowledge support from the Brazilian Instituto Nacional de Ciência e Tecnologia (INCT) do e-Universo (CNPq Grant No. 465376/2014-2). This document was prepared by the DES Collaboration using the resources of the Fermi National Accelerator Laboratory (Fermilab), a U.S. Department of Energy, Office of Science, Office of High Energy Physics HEP user facility. Fermilab is managed by Fermi Forward Discovery Group, LLC, acting under Contract No. 89243024CSC000002. This research used resources of the National Energy Research Scientific Computing Center (NERSC), a Department of Energy User Facility using NERSC Award No. HEP-ERCAP0035553.

All authors contributed to this paper and/or to the infrastructure work that made this analysis possible. W. d'A. extended the Y3 WZ methodology, developed the WZ code, carried out the measurements, performed the validation tests requested by the collaborations, and prepared the manuscript. G. B. contributed to the methodological development with innovative ideas, implemented the importance sampling, and assisted in manuscript preparation. B. Y. and G. G. implemented the SOM pipelines for the source and lens samples and contributed to the manuscript preparation. A. Alarcon helped with the statistical tests and their interpretation during the development of this work and contributed to the manuscript preparation. M. M. supervised W. d'A. throughout the development of this work. R. C. and M. G. made significant contributions to the manuscript preparation as internal reviewers for the collaboration. K. B. and I. S. contributed to the development of the Y6 Gold sample. M. Y., M. B., T. S., N. W., A. P., J. V., and M. R. contributed to the building of the Metadetect and MagLim++ samples, and J. P. produced their catalog versions. C. T. contributed to the development of CARDINAL. D. A. contributed to the development of BALROG for DES Y6. R. C. and J. F. contributed to the design of the BOSS-eBOSS mocks. E. L. evaluated the magnification coefficients for the different samples and helped with the galaxy color splitting. A. Amon, D. G., C. S., and M. T. contributed to the interpretation of the analysis as members of the DES Y6 redshift WG. A. P., S. A., M. C., D. S., A. F., and C. C. contributed to the development of this work as members of the DES Y6 SWG. The remaining authors have made contributions to this paper that include, but are not limited to, the construction of DECam and other aspects of collecting the data; data processing and calibration; catalog creation; developing broadly used methods, codes, and simulations; running the pipelines and validation tests; and promoting the science analysis.

DATA AVAILABILITY

The DES Y6 data products used in this work, as well as the full ensemble of DES Y6 Maglim++ [50] and Metadetect [58] samples described by this work, are publicly available at DES [79,80] (a) The reference samples are available at: (BOS) [81] for BOSS [33], (eBO) [80] for eBOSS [34], and DES (b) [80]. for DESI DR1 [36]. As cosmology likelihood sampling software we use cosmosis, available at (cos) [82]. Simple examples of WZ codes are available at (WZc) [83].

APPENDIX A: REALISTIC SPECTROSCOPIC MOCKS AND SMALL-SCALE SYSTEMATICS IN CARDINAL

For our fiducial analysis, we use BOSS-eBOSS mocks constructed from the MagLim++ mock sample, which reproduces the redshift distribution of the BOSS-eBOSS data. In an earlier version of this work, we relied on a different set of mocks. Specifically, we initially used a "blue" CARDINAL eBOSS ELG sample, built using the same color and magnitude cuts as the eBOSS ELG sample in the South Galactic Cap, and a "red" CARDINAL LRG sample, also reproducing BOSS/eBOSS selection [84]. In principle, realistic mocks can be used to assess the impact of 1-halo physics, as in [24]. On very small scales, effects such as halo assembly history, quenching, stochasticity, and conformity can cause deviations in the cross-correlation galaxy bias from the product of the individual autocorrelation biases. This deviation is quantified using a Pearson-like coefficient,

$$\eta_{ab}(r_{\rm p}) = \frac{w_{ab}(r_{\rm p})}{\sqrt{w_{aa}(r_{\rm p}) w_{bb}(r_{\rm p})}}, \tag{A1}$$

where a and b denote two galaxy samples with similar redshift distributions, $n(z)$. In the linear-bias regime, η_{ab} is expected to approach unity on large scales. Figure 18 shows the Pearson coefficients measured in CARDINAL as a function of scale and redshift, for different combinations of a and b. As expected, $\eta_{ab} \to 1$ for $r_{\rm p} > 10$ Mpc. However, we also observe a significant suppression of η_{ab} at $r_{\rm p} < 1.5$ Mpc, with a clear redshift dependence. Unlike in [24], we find that this suppression extends to intermediate scales ($1.5 < r_{\rm p} < 10$ Mpc), beyond the typical 1-halo regime.

Tests on the DES Y6 data (see Figs. 10 and 11) show limited differences across redshifts in the WZ results when using smaller (< 1.5 Mpc) and larger scales (> 5 Mpc). For these two figures, we use $b_{\rm r}^{w_{\rm rr}}$ as a proxi to $b_{\rm r}^{w_{\rm ur}}$, showing that any potential deviation is limited for the reference galaxy bias. For the unknown galaxy bias, we know (i) from linear theory that the large-scale $b_{\rm u}^{w_{\rm ur}}$ is equal to the large-scale $b_{\rm u}^{w_{\rm uu}}$, and (ii) $b_{\rm u}^{w_{\rm ur}}$ values are consistent between 1.5 and 15 Mpc (cf. Fig. 9); (iii) we tested galaxy bias from $w_{\rm uu}$ are consistent between 1.5 and 15 Mpc; thus we can deduce (iv) at scales $r_{\rm p} \sim 1.5$ Mpc, the $b_{\rm u}^{w_{\rm ur}}$ would be consistent with $b_{\rm u}^{w_{\rm uu}}$. In addition in Appendix B 1, we measure the η_{ab} functions for different red and blue tracer samples generated from MagLim++ and Redmagic. We observe some deviations from unity, but limited to the range $r_{\rm p} < 1.5$ Mpc and far from the factor 5 and redshift evolution observed in Fig. 18. Thus the variations of η observed in CARDINAL do not appear to be physical.

In CARDINAL, the autocorrelation properties of red and blue galaxies, as well as their mixtures, were validated against SDSS data (see Fig. 5 of [45]). However, the clustering of faint galaxies already shows significant discrepancies with the data, even at large scales. More importantly, the cross-correlation between red and blue galaxies was not validated. Therefore, the type of small-scale cross-correlation analysis we aim to perform (at ∼1 Mpc) was not reliably tested in CARDINAL. We found that the MagLim++-based mocks exhibit fewer of these issues. Although we cannot produce Fig. 18 directly from photometric data, the cross-correlations in the MagLim++ mocks appear consistent with our data measurements, as seen in Figs. 9 and 22. Consequently, we adopted the MagLim++-based mocks for our fiducial analysis. We emphasize that mocks are used to define priors on systematics—not to parametrize them precisely with informative priors. Our methodology is deliberately conservative and flexible, allowing for systematic amplitudes larger than those observed in CARDINAL. Therefore, despite concerns about mock realism, we are confident in the robustness of our results.

APPENDIX B: IMPACT OF THE COLORS OF THE REFERENCE SAMPLE

1. On small-scale systematics

The goal here is to measure $\eta_{ab}(r_{\rm p}, z)$ for combinations of blue and red galaxy samples. We use the last four MagLim++ bins and split each into blue and red

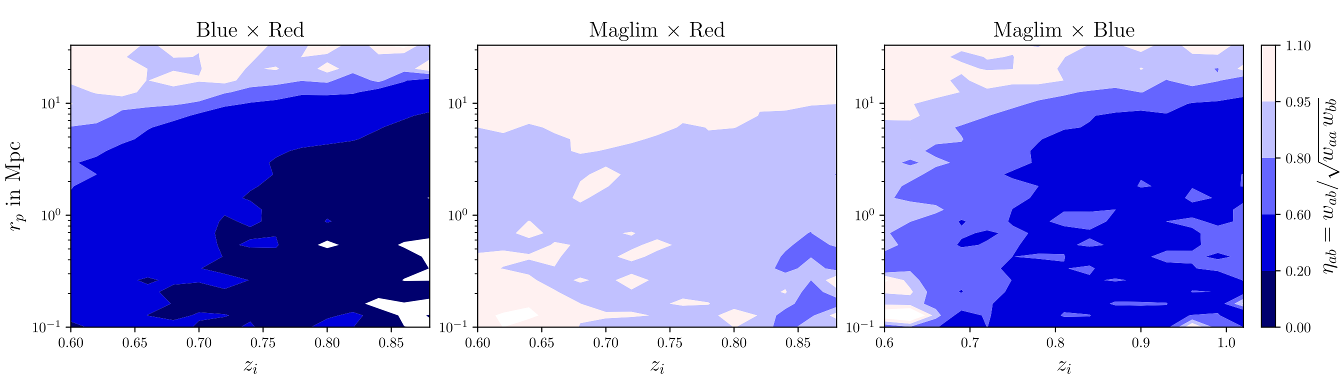

FIG. 18. Difference of the biases in the cross-correlations and the biases of the autocorrelations, quantified by a Pearson-like coefficients. We evaluate this quantity for different combinations of Mocks.

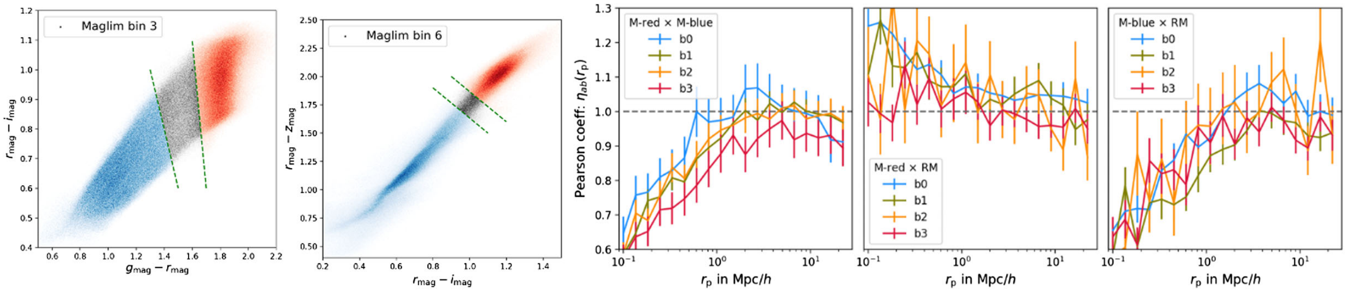

FIG. 19. Left: separation of the blue (in blue) and red (in red) samples in color space for two of the four MagLim++ bins we considered. Right: Pearson-like coefficient for the cross-correlations of the MagLim++ blue and red samples, the MagLim++ red and Redmagic samples, and the MagLim++ blue and Redmagic samples for four bin pairs b0–b3. We measure deviations from unity at $r_p < 1.5$ Mpc, but a rather constant equal to unity trend for larger scales. The cross-correlations of red and blue samples results in undercorrelations, while the cross-correlations of the two red samples seem to result in an excess.

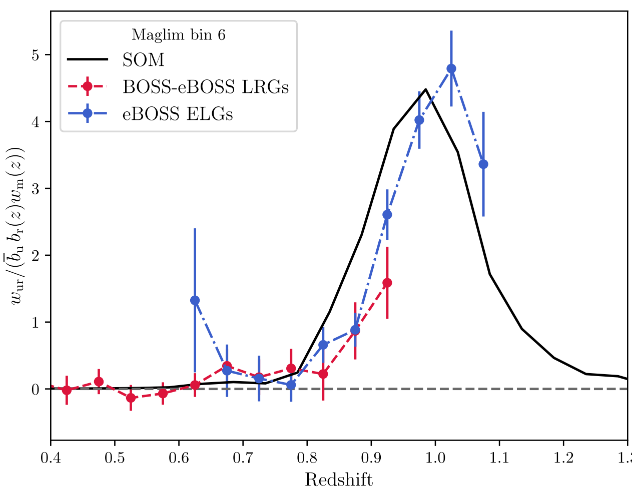

FIG. 20. WZ for the MagLim++ lens bin 6, using separately the reference red (LOWZ-CMASS-eBOSS LRG) and blue (eBOSS ELG) samples. We observe both reference sample are consistent and predict a smaller $n(z)$ at $z \sim 0.85$.

subsamples (one can find color sample split for source sample in [85] with the SOM method), isolating the color bimodality in color-color space. Two examples of this bimodality are shown in Fig. 19. In addition, we consider an extra red sample using Redmagic, but whose galaxies in common with MagLim++ have been removed to ensure independence. We then create four Redmagic bins whose redshift ranges closely match those of the four MagLim++ bins. Unlike the approach used for CARDINAL in Appendix A, here we cannot measure w_{ab}, w_{aa}, and w_{bb} for a and b within the same narrow redshift range. Therefore, we must account for differences in the redshift distributions. We estimate the $n(z)$ of each sample using BOSS-eBOSS cross-correlations on significantly larger scales ($5 < r_p < 30$ Mpc) than usual, to avoid small-scale effects, and we neglect galaxy-bias evolution. To disentangle the impact of galaxy bias from that of the redshift distribution on η, we define a modified correlation function,

$$\tilde{w}_{xy}(r_p) = \frac{\int dz n_x(z) n_y(z) \xi_{xy}(z, r_p)}{\int dz n_x(z) n_y(z) \xi_m(z, r_p)}, \tag{B1}$$

$$\eta_{ab}(r_p) = \frac{\tilde{w}_{ab}(r_p)}{\sqrt{\tilde{w}_{aa}(r_p)\tilde{w}_{bb}(r_p)}}. \tag{B2}$$

We obtain $\tilde{w}$ by dividing the measured correlations $w^{meas}_{xy}(r_p)$ by the denominator of the right term in the equation below. We only consider cross-correlations between color bins that overlap significantly in redshift. The results of the three cross-correlations (M-red × M-blue, M-red ×RM (Redmagic), M-blue ×RM) for the four bin pairs (referred as b0–b3) are shown in Fig. 19. For scales larger than 1.5 Mpc, η_{ab} is generally consistent with unity, except for bin 4 of MagLim++ red × MagLim++ blue, which shows a constant offset even at large scales, where linear theory predicts $\eta_{ab} = 1$. This behavior likely reflects a miscalibration of the individual $n(z)$ used in computing $\tilde{w}$, rather than a physical effect. For blue-red cross-correlations, we generally observe a decrease in η at small scales, as expected since blue and red galaxies tend to occupy different halos (see discussion in Sec. 4.3 of [24]). Interestingly, for the two distinct red samples, we measure an increase in η at small scales.

All the trends we observe are far from the extreme behaviors seen in CARDINAL (Appendix A), where $\eta \sim 0.2$ even at $r_p \sim 5$ Mpc. This validates our choice to switch to the second set of BOSS-eBOSS mocks, which ended up mitigating this effect in CARDINAL.

2. On MagLim++ bin 6 WZ

For the last MagLim++ bin, WZ predicts a significantly smaller $n(z)$ than the SOM estimate around $z \sim 0.85$. This redshift corresponds to the transition in the reference sample r from LRGs to ELGs. We evaluate correlations on small scales, where environmental effects can play an important role. In particular, if $b_u^{w_{ur}}$ differs at small scales when r is composed solely of LRGs vs solely of ELGs, this could introduce a nonphysical jump in the inferred $n_u(z)$

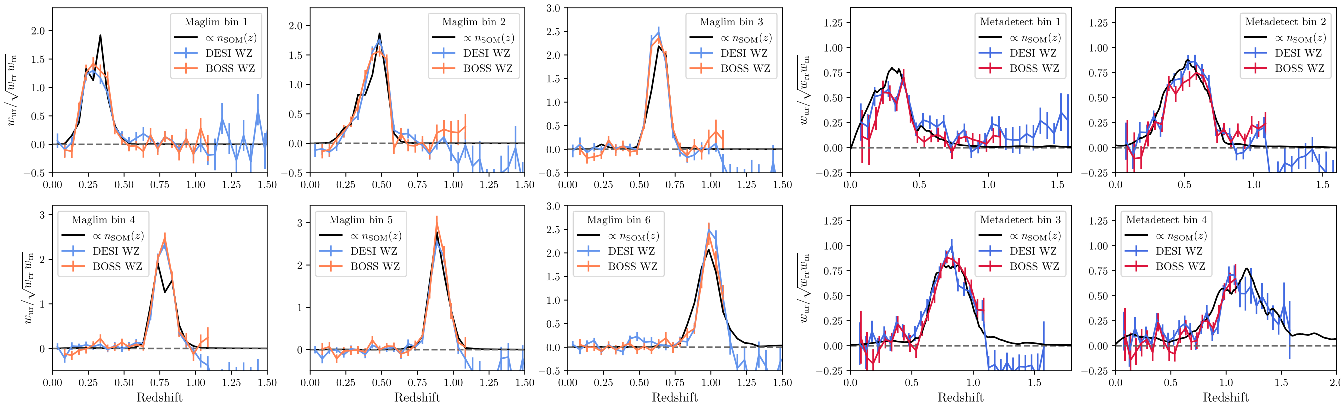

FIG. 21. WZ measurements using DESI and BOSS-eBOSS galaxy samples, for the six MagLim++ bins and the four Metadetect bins. We observe an excellent agreement.

near the LRG-ELG transition [24]. To test this, we perform WZ measurements separately for BOSS + eBOSS LOWZ-CMASS-LRGs and for eBOSS ELGs, as recommended by d'Assignies *et al.* [24], assuming a fixed value of $b_{\rm u} = 2$. The results are shown in Fig. 20. We find good agreement between the two measurements, ruling out the reference tracer type as the cause of the low $n(z)$ observed in this bin.

APPENDIX C: DESI WZ

In this section, we report the $n(z)$ using DESI DR1 galaxies as reference samples (for a DESI-DR2 WZ analysis of hyper-suprime-cam data see [78]. In short, we use DESI BGS, LRGs, ELGs, up to $z = 1.6$ [36]. We obtain a sky overlap with DES of 800 deg^2, with a slightly different footprint than BOSS-eBOSS. The WZ measurements are performed over 1.5–5 Mpc, and reported in Fig. 21. For the six MagLim++ bins, the agreement with BOSS-eBOSS is excellent. For Metadetect the agreement also appears very good, but with more deviations, such as the excess of $n(z)$ for the first bin at $z = 0.55$. With a simple shift and stretch model, we found the mean-z inferred from DESI to be consistent with the one from BOSS-eBOSS for every bin. We also observe in Fig. 21 that a magnification-like-effect seems to be large for ELG, at $z > 1$, as we measured $w_{\rm ur} < 0$. Fiber collisions, which are particularly relevant for ELGs in DESI-DR1, could also contribute to this behavior. Including DESI WZ would require an estimate of the magnification coefficients, test of the validity of the scale range, and new sys priors, as our measurement now extend up to $z = 1.6$. The photometric redshift uncertainty is not the most limiting systematics for DES Y6, as explained in Sec. IV D. Thus, in order to avoid delaying the DES Y6 analysis, we did not include these DESI measurement to the official pipeline.

APPENDIX D: IMPACT OF THE SCALE RANGES ON WZ

In Sec. IV B 2, we evaluated the WZ measurements using three different scale ranges: small scales, [0.1, 1.5] Mpc;

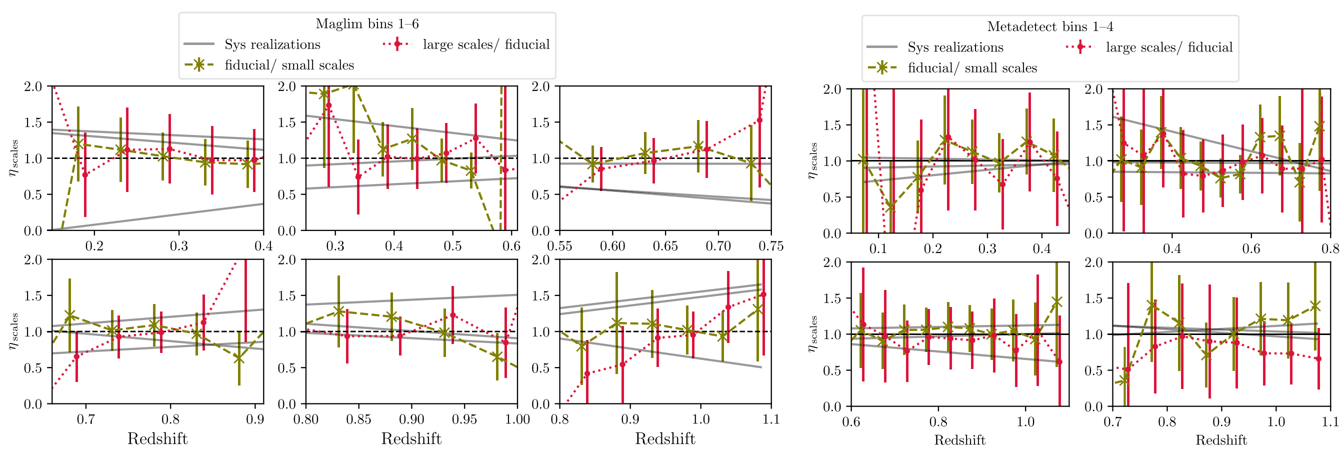

FIG. 22. Ratio of the $n(z)$ inferred from different scale ranges for the six MagLim++ bins (right) and the four Metadetect bins (left). The redshift range for every panel was chosen to remove all the points corresponding to small $n(z)$, as evaluating ratios for those is not relevant. The fiducial scales/small scales are reported in green and the large-scale/fiducial in red. We report as well some realizations of the Sys functions given our priors measured in Figs. 5 and 4.

fiducial range, [1.5, 5] Mpc; large scales, [5, 15] Mpc, and we estimate the redshift distributions, neglecting magnification and systematics. To quantify any scale-dependent deviations, we compute the ratio of the inferred redshift distributions between different scale ranges: $\eta_{\mathrm{scales}}(z) = n(z|\mathrm{scales}_1)/n(z|\mathrm{scales}_2)$. The results are shown in Fig. 22. We observe no statistical deviation from unity for the large-scale/fiducial ratio, validating our scale-range choice. More surprisingly, we also do not observe significant deviation using the smaller-scale range, this measurement being associated with higher SNR. We also report few realizations of the systematic functions, randomly sampling over our Gaussian priors, and observe that our systematic function can describe these kind of (nonsignificant) variations.

[1] R. Bordoloi, S. J. Lilly, and A. Amara, Mon. Not. R. Astron. Soc. **406**, 881 (2010).
[2] H. Hildebrandt *et al.*, Astron. Astrophys. **647**, A124 (2021).
[3] D. Huterer, M. Takada, G. Bernstein, and B. Jain, Mon. Not. R. Astron. Soc. **366**, 101 (2006).
[4] B. Stölzner, B. Joachimi, A. Korn, H. Hildebrandt, and A. H. Wright, Astron. Astrophys. **650**, A148 (2021).
[5] G. Desprez *et al.* (Euclid Collaboration), Astron. Astrophys. **644**, A31 (2020).
[6] O. Ilbert *et al.* (Euclid Collaboration), Astron. Astrophys. **647**, A117 (2021).
[7] M. Salvato, O. Ilbert, and B. Hoyle, Nat. Astron. **3**, 212 (2019).
[8] M. Tanaka, J. Coupon, B.-C. Hsieh, S. Mineo, A. J. Nishizawa, J. Speagle, H. Furusawa, S. Miyazaki, and H. Murayama, Publ. Astron. Soc. Jpn. **70**, S9 (2018).
[9] A. Campos *et al.*, arXiv:2408.00922.
[10] G. Giannini *et al.*, Mon. Not. R. Astron. Soc. **527**, 2010 (2024).
[11] C. Sánchez, M. Raveri, A. Alarcon, and G. M. Bernstein, Mon. Not. R. Astron. Soc. **498**, 2984 (2020).
[12] A. H. Wright, H. Hildebrandt, J. L. van den Busch, and C. Heymans, Astron. Astrophys. **637**, A100 (2020).
[13] A. H. Wright, H. Hildebrandt, J. L. van den Busch, C. Heymans, B. Joachimi, A. Kannawadi, and K. Kuijken, Astron. Astrophys. **640**, L14 (2020).
[14] W. G. Hartley *et al.*, Mon. Not. R. Astron. Soc. **496**, 4769 (2020).
[15] R. Cawthon *et al.*, Mon. Not. R. Astron. Soc. **513**, 5517 (2022).
[16] M. Gatti *et al.*, Mon. Not. R. Astron. Soc. **477**, 1664 (2018).
[17] M. Gatti *et al.*, Mon. Not. R. Astron. Soc. **510**, 1223 (2022).
[18] M. McQuinn and M. White, Mon. Not. R. Astron. Soc. **433**, 2857 (2013).
[19] B. Ménard *et al.*, arXiv:1303.4722.
[20] C. B. Morrison, H. Hildebrandt, S. J. Schmidt, I. K. Baldry, M. Bilicki, A. Choi, T. Erben, and P. Schneider, Mon. Not. R. Astron. Soc. **467**, 3576 (2017).
[21] J. A. Newman, Astrophys. J. **684**, 88 (2008).
[22] M. M. Rau, R. Dalal, T. Zhang, X. Li, A. J. Nishizawa, S. More, R. Mandelbaum, H. Miyatake, M. A. Strauss, and M. Takada, Mon. Not. R. Astron. Soc. **524**, 5109 (2023).
[23] V. Scottez, A. Benoit-Lévy, J. Coupon, O. Ilbert, and Y. Mellier, Mon. Not. R. Astron. Soc. **474**, 3921 (2018).
[24] W. d'Assignies *et al.*, Astron. Astrophys. **702**, A155 (2025).
[25] J. L. van den Busch *et al.*, Astron. Astrophys. **642**, A200 (2020).
[26] K. Naidoo *et al.*, Astron. Astrophys. **670**, A149 (2023).
[27] B. Yin *et al.*, arXiv:2510.23566.
[28] G. Giannini and A. Alarcon *et al.*, arXiv:2509.07964.
[29] G. Bernstein *et al.*, arXiv:2506.00758.
[30] S. Mau *et al.* (to be published).
[31] G. Giannini *et al.*, arXiv:2601.15175.
[32] S. J. Schmidt, B. Ménard, R. Scranton, C. Morrison, and C. K. McBride, Mon. Not. R. Astron. Soc. **431**, 3307 (2013).
[33] K. S. Dawson *et al.*, Astron. J. **145**, 10 (2013).
[34] K. S. Dawson *et al.*, Astron. J. **151**, 44 (2016).
[35] E. Rozo *et al.*, Mon. Not. R. Astron. Soc. **461**, 1431 (2016).
[36] A. G. Adame *et al.*, J. Cosmol. Astropart. Phys. 07 (2025) 017.
[37] E. Krause *et al.*, arXiv:2105.13548.
[38] J. Elvin-Poole *et al.*, Mon. Not. R. Astron. Soc. **523**, 3649 (2023).
[39] E. Legnani *et al.*, arXiv:2601.14833.
[40] N. E. Chisari *et al.*, Astrophys. J. Suppl. Ser. **242**, 2 (2019).
[41] D. Blas, J. Lesgourgues, and T. Tram, J. Cosmol. Astropart. Phys. 07 (2011) 034.
[42] R. Takahashi, M. Sato, T. Nishimichi, A. Taruya, and M. Oguri, Astrophys. J. **761**, 152 (2012).
[43] Euclid Collaboration, Astron. Astrophys. **697**, A5 (2025).
[44] H. Hildebrandt, Mon. Not. R. Astron. Soc. **455**, 3943 (2016).
[45] C.-H. To *et al.*, Astrophys. J. **961**, 59 (2024).
[46] M. Davis and P. J. E. Peebles, Astrophys. J. **267**, 465 (1983).
[47] S. D. Landy and A. S. Szalay, Astrophys. J. **412**, 64 (1993).
[48] M. Jarvis, TreeCorr: Two-point correlation functions, Astrophysics Source Code Library, record ascl:1508.007.
[49] J. Hartlap, P. Simon, and P. Schneider, Astron. Astrophys. **464**, 399 (2007).
[50] N. Weaverdyck and M. Rodríguez-Monroy *et al.*, 2026.
[51] R. Buchs *et al.*, Mon. Not. R. Astron. Soc. **489**, 820 (2019).
[52] J. Myles *et al.*, Mon. Not. R. Astron. Soc. **505**, 4249 (2021).
[53] C. Sánchez *et al.*, Mon. Not. R. Astron. Soc. **525**, 3896 (2023).
[54] D. Anbajagane and M. Tabbutt *et al.*, 2025.
[55] J. R. Weaver *et al.*, Astrophys. J. Suppl. Ser. **258**, 11 (2022).
[56] A. Alarcon *et al.*, Mon. Not. R. Astron. Soc. **501**, 6103 (2021).
[57] D. Navarro-Gironés *et al.*, Mon. Not. R. Astron. Soc. **534**, 1504 (2024).

[58] M. Yamamoto *et al.*, Mon. Not. R. Astron. Soc. **543**, 4156 (2025).
[59] K. Bechtol *et al.*, 2025.
[60] M. Rodríguez-Monroy and N. Weaverdyck *et al.*, arXiv: 2509.07943.
[61] T. Schutt *et al.*, Open J. Astrophys. **8**, 26 (2025).
[62] J. De Vicente, E. Sánchez, and I. Sevilla-Noarbe, Mon. Not. R. Astron. Soc. **459**, 3078 (2016).
[63] A. Porredon *et al.*, Phys. Rev. D **106**, 103530 (2022).
[64] N. Weaverdyck *et al.* (to be published).
[65] E. F. Schlafly, A. M. Meisner, and G. M. Green, Astrophys. J. Suppl. Ser. **240**, 30 (2019).
[66] N. Palanque-Delabrouille *et al.*, Astron. Astrophys. **587**, A41 (2016).
[67] A. J. Ross *et al.*, Mon. Not. R. Astron. Soc. **498**, 2354 (2020).
[68] C.-H. To *et al.* (to be published).
[69] J. DeRose *et al.*, arXiv:1901.02401.
[70] M. R. Blanton *et al.*, Astron. J. **129**, 2562 (2005).
[71] M. R. Becker, PhD thesis, University of Chicago, 2013.
[72] M. Martinelli *et al.*, Astron. Astrophys. **649**, A100 (2021).
[73] A. Nicola *et al.*, J. Cosmol. Astropart. Phys. 02 (2024) 015.
[74] M. Kerscher, I. Szapudi, and A. S. Szalay, Astrophys. J. **535**, L13 (2000).
[75] M. Vargas-Magaña *et al.*, Astron. Astrophys. **554**, A131 (2013).
[76] Euclid Collaboration, Astron. Astrophys. **697**, A1 (2025).
[77] The LSST Dark Energy Science Collaboration, arXiv:1809 .01669.
[78] J. Choppin de Janvry *et al.*, arXiv:2511.18133.
[79] https://des.ncsa.illinois.edu/releases.
[80] https://data.sdss.org/sas/dr17/eboss/lss/catalogs/DR16/.
[81] https://data.sdss.org/sas/dr12/boss/lss/.
[82] https://github.com/joezuntz/cosmosis.
[83] https://github.com/wdassignies/Clustering_z.
[84] A. Raichoor *et al.*, Mon. Not. R. Astron. Soc. **471**, 3955 (2017).
[85] J. McCullough *et al.*, arXiv:2410.22272.